

Mobility of 2D materials from first principles in an accurate and automated framework

Thibault Sohier,¹ Davide Campi,¹ Nicola Marzari,¹ and Marco Gibertini^{1,2}

¹*Theory and Simulation of Materials (THEOS), and National Centre for Computational Design and Discovery of Novel Materials (MARVEL), École Polytechnique Fédérale de Lausanne, CH-1015 Lausanne, Switzerland*

²*Department of Quantum Matter Physics, University of Geneva, CH-1211 Geneva, Switzerland*
(Dated: November 26, 2018)

We present a first-principles approach to compute the transport properties of 2D materials in an accurate and automated framework. We use density-functional perturbation theory in the appropriate bidimensional setup with open-boundary conditions in the third direction. The materials are charged by field effect via planar counter-charges. In this approach, we obtain electron-phonon matrix elements in which dimensionality and doping effects are inherently accounted for, without the need for post-processing corrections. This treatment highlights some unexpected consequences, such as an increase of electron-phonon coupling with doping in transition-metal dichalcogenides. We use symmetries extensively and identify pockets of relevant electronic states to minimize the number of electron-phonon interactions to compute; the integrodifferential Boltzmann transport equation is then linearized and solved beyond the relaxation-time approximation. We apply the entire protocol to a set of much studied materials with diverse electronic and vibrational band structures: electron-doped MoS₂, WS₂, WSe₂, phosphorene, arsenene, and hole-doped phosphorene. Among these, hole-doped phosphorene is found to have the highest mobility, with a room temperature value around 600 cm²·V⁻¹·s⁻¹. Last, we identify the factors that affect most phonon-limited mobilities, such as the number and the anisotropy of electron and hole pockets, to provide a broader understanding of the driving forces behind high mobilities in two-dimensional materials.

I. INTRODUCTION

The scientific and engineering community is devoting a major effort towards the identification and fabrication of novel 2D materials^{1–11} and their application in electronic devices^{12,13}. To accelerate the discovery of the best candidates for electronic transport, systematic and accurate methods to compute phonon-limited resistivity and mobility from first principles would be very beneficial. Nevertheless, these quantities are not straightforward to compute and various degrees of approximations are often needed.

A very successful approach relies on the solution of the Boltzmann transport equation^{14,15} (BTE), in which the electron-phonon coupling (EPC) enters the expression for the scattering rates^{16,17} and can be computed from first principles within density-functional perturbation theory (DFPT)^{18–22} or with finite-differences schemes^{23,24}. Although both methods proved to be very successful, DFPT is more efficient in dealing with long-wavelength effects since it does not need large supercells to accommodate the perturbation, and will thus be the method of choice in the following.

Either way, the computation of EPC in 2D materials from first principles presents some challenges. Being ruled by long-range Coulomb interactions, the long-wavelength electron-phonon dynamics are highly dependent on dimensionality. The most obvious example is the Fröhlich interaction in polar materials, which diverges in the long-wavelength limit in 3D while remains finite in 2D²⁵. This fundamentally different behaviour is difficult to capture in standard electronic-structure codes based on plane-wave basis sets because of the spurious interaction with artificial periodic images, which leads to erro-

neous results when $\mathbf{q} \rightarrow 0$. Thus, special care must be adopted when computing the response of a 2D system to long-wavelength perturbations^{25–28}.

An appropriate treatment of doping is an additional challenge. While field-effect charging is omnipresent in experimental setups, it is usually not included in first-principles simulations. Often, calculations are performed for the neutral case, and the Fermi level is shifted within a frozen-band approximation when integrating the EPC matrix elements to obtain a certain scattering-related quantity. This is approximate because the EPC itself depends on doping, most notably via screening, but also via other mechanisms that will be discussed later. A more realistic description is now possible thanks to a recent development of DFPT for gated 2D materials²⁹, where the doping charge is neutralized by adding planar distributions of counter-charges, mimicking experimental conditions where 2D materials are doped electrostatically through gates.

Another source of challenge is that, in general, a very large number of EPC matrix elements must be computed to obtain a fine enough sampling of the electron-phonon dynamics over the Brillouin zone, which is computationally very expensive. To boost efficiency, one may use Wannier interpolations^{30–35} to obtain inexpensively the EPC over a dense mesh. However, interpolations work seamlessly only with short-range interactions. Long-range effects, such as Fröhlich or piezo-electric coupling, need to be modeled and treated separately; this has been solved for three-dimensional systems^{36,37}, while in 2D, Fröhlich coupling has been modeled²⁵ and efficient ways to interpolate the phonon dispersions have been put forward²⁸, but a thorough description of EPC interpolation is still missing. Nonetheless, the absence of interpo-

lation techniques might not be, in the long run, a major constraint. Indeed, the reduced dimensionality entails one less dimension to sample, with a drastic reduction of electronic states and phonons to consider. Thus, it can be argued that for 2D materials, one should focus on addressing dimensionality and charging first, rather than interpolation.

Here, we thus choose a direct approach and compute all EPC matrix elements from DFPT in the appropriate boundary and charging conditions²⁹. The use of symmetries and energy selection rules, in addition to the momenta being restricted to two dimensions, makes the process computationally feasible.

For the solution to the Boltzmann transport equation for electrons and holes, different approaches involving various degrees of approximation have been put forward. In the case of metals, Allen derived an approximate solution¹⁵ by suitably modifying Eliashberg theory¹⁶ to transport. This approach has been successfully applied in the early efforts to compute mobilities from first principles^{21,38} and it is now customary in many available transport codes such as EPW³⁵. In the general case, including semiconductors, the major challenge is that the integrodifferential BTE does not have a closed-form solution. Most approaches use then some form of relaxation-time approximation^{24,39–49} to obtain a closed-form result.

Still, the errors associated with the various approximate solutions to the BTE in the literature are often difficult to quantify. An iterative scheme inspired by the original Rode's method^{50,51} to solve the inelastic part of the BTE has been recently proposed^{52–55}, while a very efficient preconditioned conjugate-gradient approach has been reported in Ref. 56 following a recipe introduced in the context of the phonon Boltzmann equation for thermal transport^{57–59}. Ref. 54 also offers an interesting comparison of the different methods to solve the BTE and shows a broad agreement between these for the case of MoS₂; still, this might not be the case for all materials. A full numerical solution of the BTE beyond the relaxation-time approximation was introduced in Ref. 60 for graphene. An advantage of this latter method is that it does not require a broadening of the δ functions enforcing energy selection rules, contrary to the other methods mentioned above. It was, however, tailored specifically for graphene. Here, we propose a more general approach with iterative scheme combined with the use of the triangles method^{61,62} for accurate integrations of the δ functions.

Relatively few 2D materials have had mobilities theoretically investigated up to now. Graphene has been studied extensively^{24,40,41,43,44,60,63–75}, showing excellent agreement⁴⁴ with experiments¹ and a detailed understanding of the main processes limiting mobility⁴¹, including the effects of dimensionality and charging by field effect^{29,75}. MoS₂, another prototypical 2D material, has also been studied in several works^{24,42,43,52–54}, as well as phosphorene^{45–48,76,77}, arsenene^{78–80}, silicene²⁴, and

other TMDs⁴². On the other hand, the effects of periodic images and dimensionality are explicitly treated only in some of the first-principles efforts^{24,52,53}. Charging is most often treated as a rigid shift of the Fermi energy in the computation of the transport properties, but not included in the computation of the matrix elements themselves. Consequently, the influence of doping on the EPC is generally neglected. In some instances, electronic screening is accounted for analytically^{52,53}, but this necessarily entails the use of models and approximations (not obvious in 2D). Also, as will be shown here, screening is not the only effect of doping on EPC matrix elements. Last, computational accuracy is often limited by the very expensive nature of the Brillouin zone (BZ) integrals. For all these reasons, a full treatment of doping and periodicity is necessary, together with an efficient and automatic implementation of all BZ sums.

All these points are addressed in this paper, that is structured as follows. In the first section, we describe the formal framework of the BTE and identify the quantities needed to solve it. In the second section, we present the workflow of first-principles calculations used to compute the physical quantities associated with phonon-limited transport. Then, we discuss the results of this workflow applied to a set of known prototypical materials, i.e., three electron-doped TMDs in their 2H form (MoS₂, WS₂, WSe₂), as well as electron-doped (gray) arsenene, and both hole- and electron-doped (black) phosphorene.

II. BOLTZMANN TRANSPORT EQUATION

In this first section, we review the framework of the Boltzmann transport equation for electrons in an effort to settle the context and introduce the various quantities used in the rest of the paper. Similar derivations can be found in the literature, e.g. in Ref. 14, 81, and 82. We consider any 2D material to lie in the $x-y$ plane with an applied electric field in the same plane, in the $-\mathbf{u}_E$ direction. The electric field favors states with wavevectors \mathbf{k} in the opposite direction, \mathbf{u}_E , thus taking the electronic distribution f out of its equilibrium Fermi-Dirac ground-state f^0 . Phonon scattering acts to bring the system back towards its unperturbed equilibrium state; then, a steady-state regime is reached and a net electric current \mathbf{j} emerges. The conductivity, or the inverse of the resistivity, is then defined as^{14,81,82}:

$$\sigma = \frac{1}{\rho} = \sum_{\alpha} \frac{2e}{|\mathbf{E}|} \int_{k \in \alpha} \frac{d\mathbf{k}}{(2\pi)^2} f(\mathbf{k}) \mathbf{v}(\mathbf{k}) \cdot \mathbf{u}_E \quad (1)$$

where the factor 2 accounts for spin degeneracy, $e > 0$ is the Coulomb charge, \mathbf{E} the electric field, α is an index representing the different valleys in the Brillouin zone, $f(\mathbf{k})$ is the steady-state occupation function, and $\mathbf{v}(\mathbf{k})$ the band velocity of the electronic state. Here, rather than integrating over all the Brillouin zone, we limit ourselves to the relevant electron or hole pockets that are

occupied by temperature or doping. In semiconductors, these pockets form valleys which we will further define later, and wavevectors \mathbf{k} are taken from these valleys. Mobilities can then be obtained from the Drude model as $\mu = \sigma/n$, where n is the electron density (replace with hole density p in the case of hole doping). The central quantity to obtain is thus the occupation distribution $f(\mathbf{k})$. Assuming this to be spatially uniform and time-independent (steady-state), the Boltzmann transport equation states that the change of the occupation distribution driven by the electric field must be compensated by scattering^{14,81,82}:

$$-\frac{e\mathbf{E}}{\hbar} \cdot \frac{\partial f}{\partial \mathbf{k}} = \left(\frac{\partial f}{\partial t} \right)_{\text{scatt}}(\mathbf{k}) \quad (2)$$

The collision integral (right-hand side) can be found using Fermi's golden rule:

$$\left(\frac{\partial f}{\partial t} \right)_{\text{scatt}}(\mathbf{k}) = \sum_{\mathbf{k}'} P_{\mathbf{k}'\mathbf{k}} f(\mathbf{k}') (1 - f(\mathbf{k})) - P_{\mathbf{k}\mathbf{k}'} f(\mathbf{k}) (1 - f(\mathbf{k}')), \quad (3)$$

where $P_{\mathbf{k}\mathbf{k}'}$ is the scattering probability from state \mathbf{k} to state \mathbf{k}' ; $P_{\mathbf{k}\mathbf{k}'}$ should include in general all relevant scattering processes. Here, we sum over all electron-phonon scattering probabilities associated with the phonons modes of the system, i.e. $P_{\mathbf{k}\mathbf{k}'} = \sum_{\nu} P_{\mathbf{k}\mathbf{k}',\nu}$, where $P_{\mathbf{k}\mathbf{k}',\nu}$ is the sum of phonon emission and absorption terms¹⁶ for phonon mode ν of momentum $\mathbf{q} = \mathbf{k}' - \mathbf{k}$:

$$P_{\mathbf{k}\mathbf{k}+\mathbf{q},\nu} = \frac{2\pi}{\hbar} \frac{1}{N} |g_{\mathbf{k}\mathbf{k}+\mathbf{q},\nu}|^2 \{ n_{\mathbf{q},\nu} \delta(\varepsilon_{\mathbf{k}+\mathbf{q}} - \varepsilon_{\mathbf{k}} - \hbar\omega_{\mathbf{q},\nu}) + (n_{\mathbf{q},\nu} + 1) \delta(\varepsilon_{\mathbf{k}+\mathbf{q}} - \varepsilon_{\mathbf{k}} + \hbar\omega_{\mathbf{q},\nu}) \}. \quad (4)$$

In the expression above, $g_{\mathbf{k}\mathbf{k}+\mathbf{q},\nu}$ is the electron-phonon coupling (EPC) matrix element and $n_{\mathbf{q},\nu}$ is the phonon occupation, which we assume to be the equilibrium Bose-Einstein distribution. The δ functions stem from the energy selection rules involved in scattering, forcing the need to evaluate the EPC on very fine momentum grids, making the calculations challenging. Phonon scattering as described in Eq. 4 involves three quasi-particles: an initial electronic state, a final electronic state, and a phonon. The EPC matrix element connecting the initial and final states can be computed within DFPT^{17,22} and reads:

$$g_{\mathbf{k},\mathbf{k}+\mathbf{q},\nu} = \sum_{a,i} e_{\mathbf{q},\nu}^{a,i} \sqrt{\frac{\hbar}{2M_a\omega_{\mathbf{q},\nu}}} \langle \mathbf{k} + \mathbf{q} | \frac{\partial V_{\text{KS}}(\mathbf{r})}{\partial \mathbf{u}_{a,i}(\mathbf{q})} | \mathbf{k} \rangle \quad (5)$$

where a is an atomic index, i a cartesian index, $e_{\mathbf{q},\nu}^{a,i}$ is the phonon eigenvector, M_a is the mass of atom a , $|\mathbf{k}\rangle, |\mathbf{k}+\mathbf{q}\rangle$ are the initial and final electronic states, and $\frac{\partial V_{\text{KS}}(\mathbf{r})}{\partial \mathbf{u}_{a,i}(\mathbf{q})}$ is the derivative of the Kohn-Sham potential with respect to a periodic displacement of atom a in direction i .

We adopt a perturbation approach at first order in electric field and write :

$$f(\mathbf{k}) = f^0(\mathbf{k}) + f^1(\mathbf{k}) \quad (6)$$

where $f^0(\mathbf{k})$ is the Fermi-Dirac function and $f^1(\mathbf{k})$ is the linear perturbation proportional to the electric field, for which it is convenient to make the following general ansatz

$$f^1(\mathbf{k}) = e|\mathbf{E}|\mathbf{u}_{\mathbf{E}} \cdot \mathbf{F}(\mathbf{k}) \frac{\partial f^0(\mathbf{k})}{\partial \varepsilon} \quad (7)$$

where $\mathbf{F}(\mathbf{k})$ is a vectorial quantity with units of length that can be understood as a mean free displacement⁵⁴. In the following the only approximation we make is to assume that this mean free displacement is along the band velocity, that is we write:

$$\mathbf{F}(\mathbf{k}) = \mathbf{v}(\mathbf{k})\tau(\mathbf{k}) \quad (8)$$

where $\tau(\mathbf{k})$ is unknown and has the dimension of time. We will call it scattering time, although it is *not* the scattering time as often understood in the context of the relaxation-time approximation. This is similar to what has been proposed by Rode^{50,51}, and reduces to his trial solution when $\mathbf{v}(\mathbf{k}) \propto \mathbf{k}$.

By replacing the occupation distribution of Eq. 6 with the ansatz Eq. 7 and 8 in Eq. 9, and keeping only first-order terms in the electric field, we get to what we will refer to as the linearized BTE:

$$(1 - f^0(\mathbf{k}))\mathbf{v}(\mathbf{k}) \cdot \mathbf{u}_{\mathbf{E}} = \sum_{\mathbf{k}'} P_{\mathbf{k}\mathbf{k}'} (1 - f^0(\mathbf{k}')) \times \{ \mathbf{v}(\mathbf{k}) \cdot \mathbf{u}_{\mathbf{E}} \tau(\mathbf{k}) - \mathbf{v}(\mathbf{k}') \cdot \mathbf{u}_{\mathbf{E}} \tau(\mathbf{k}') \} \quad (9)$$

where we have used the detailed balance condition $P_{\mathbf{k}'\mathbf{k}} f^0(\mathbf{k}') (1 - f^0(\mathbf{k})) = P_{\mathbf{k}\mathbf{k}'} f^0(\mathbf{k}) (1 - f^0(\mathbf{k}'))$ and the fact that $\frac{\partial f^0(\varepsilon_{\mathbf{k}})}{\partial \varepsilon} = -\frac{f^0(\mathbf{k})(1-f^0(\mathbf{k}))}{kT}$. In Eq. 9 we keep the term $(1 - f^0(\mathbf{k}))\mathbf{v}(\mathbf{k})$ on the left-hand side to avoid having it on the right-hand side as a denominator, which would bring some numerical instability in the process of solving the equation numerically. Putting back the distribution Eq. 6 in the expression for the conductivity Eq. 1 we get:

$$\sigma = \frac{1}{\rho} = \sum_p 2e^2 \int_{k \in \alpha} \frac{d\mathbf{k}}{(2\pi)^2} (\mathbf{v}(\mathbf{k}) \cdot \mathbf{u}_{\mathbf{E}})^2 \tau(\mathbf{k}) \frac{\partial f^0}{\partial \varepsilon} \quad (10)$$

A very minimal set of approximations have been made to get to Eq. 9 and 10 (linear order in electric field, steady state, equilibrium phonon distribution, mean free displacement along band velocity). We will compute the conductivity at this level of approximation. This goes beyond the relaxation time approximation, which would correspond to neglecting the second term in brackets on the right-hand side of Eq. 9, and differs from the approaches in Ref. 54 and 56 only in the assumption of

Eq. 8. In our approach we solve the linearized BTE (Eq. 9) iteratively starting from a guess inspired by the relaxation-time approximation (see App. I), as suggested initially by Rode^{50,51}. In addition to some differences in the formulation of the BTE and the sampling of electronic and phonon momenta, our improvement with respect to the existing literature is the use of the triangles method^{61,62} to integrate the delta functions of Eq. 4.

III. WORKFLOW / CALCULATIONS

In this section we describe the computational workflow developed to calculate the transport properties of 2D materials. Electron-doped WS₂ ($n = 5 \times 10^{13} \text{ cm}^{-2}$) is used as a case study; this is a relatively complex system due to its multi-valley nature. As illustrated in Fig. 1a), the process can be separated into the two following steps:

- EPC: We compute the linear response of the system with respect to a set of phonon momenta \mathcal{Q} (defined in the following section, along with all other sets of wave vectors, \mathcal{I} and \mathcal{F}). The resulting EPC matrix elements $g_{\mathbf{k},\mathbf{k}'}^2$ are then projected on a set \mathcal{I} of relevant initial states $\mathbf{k} \in \mathcal{I}$ and interpolated on a set \mathcal{F} of final states $\mathbf{k}' \in \mathcal{F}$. The initial states are where we want to evaluate the scattering time. Final states are all the states accessible from the initial states via phonon scattering.
- Transport: The matrix elements are then used to compute the scattering probabilities $P_{\mathbf{k},\mathbf{k}'}$ and solve the BTE, which yields the scattering time for each initial state in \mathcal{I} . The scattering time is then interpolated for all states in \mathcal{F} , as shown in Fig. 1c). The integration of the scattering times gives the transport quantities, like the temperature-dependent mobilities and resistivities shown in Fig. 1 d).

In the following we first detail and justify the sampling choices for the momentum sets \mathcal{I} , \mathcal{F} and \mathcal{Q} . Then we describe each of the two steps outlined above.

A. Sampling

Phonon scattering involves three quasiparticles: an initial electronic state, a final electronic state and a phonon. We use a different momentum sampling over the Brillouin zone (BZ) for each of those quasiparticles, according to their use in the workflow and the cost of the associated calculations.

Only a subset of the electronic states are relevant for transport. We see from the expression of conductivity (Eq. 10) that one needs to find the dependency of the perturbed distribution only for electronic states for which $\frac{\partial f^0(\epsilon_{\mathbf{k}})}{\partial \epsilon}$ is significantly different from zero: this represents a set of electronic states with energies in a range of a few kT around the Fermi level. Furthermore, we see in the

collision integral that the scattering time at \mathbf{k} depends on the scattering time of possible final states at \mathbf{k}' . This means that the energy range where we need to evaluate $\tau(\mathbf{k})$ must be extended by the maximum phonon energy $\hbar\omega_{\text{max}}$ above and below. Such constraints define pockets or valleys in the BZ, and in WS₂ we keep all electronic states up to an energy 0.24 eV above the bottom of the conduction band. Panel c) of Fig. 1 shows these valleys in the Brillouin zone for WS₂. We distinguish two kinds of valleys: two K-valleys around the high-symmetry points K and K', and six valleys around the Q points, situated approximately halfway between Γ and K.

We define a fine grid \mathcal{F} on the pockets, see Fig. 2, on which quantities related to the band structure, i.e. energies and velocities, are computed. A fine grid is needed to evaluate the velocities (as gradients of the energies) properly and to converge the integrals in Eq. 9 and Eq. 10. To compute the eigenenergies on a fine grid, the ground-state electronic density is first computed on a relatively coarse grid ($32 \times 32 \times 1$); then, non self-consistent calculations are performed on a finer grid. Since the second step is relatively inexpensive, one can afford very fine sampling. We always define the grid such that the distance between two consecutive k-points is 0.01 \AA^{-1} (or as close as possible to this value using a Monkhorst-Pack mesh). For example, in WS₂, this corresponds to 226×226 k-points. The scattering times are interpolated on this grid and integrated to get the conductivity, resistivity, or mobility, as shown in Fig. 1c-d). In this work, more focused on accurate linear response, band structures are computed within DFT. However, the same approach could use bands computed at a higher level of theory, such as hybrid functionals, many-body perturbation theory (e.g. GW associated with a Wannier interpolation technique³⁴), or applying a correction to the fundamental band-gap obtained from an evaluation of the derivative discontinuity as in GLLBsc functionals^{83,84}, or even bands fitted to experiments^{85,86}.

As written in Eq. 9, the linearized BTE gives the value of $\tau(\mathbf{k})$ at an initial state \mathbf{k} as a function of $\tau(\mathbf{k}')$ at all possible final states \mathbf{k}' linked to the initial state by a phonon-scattering event. As will be explained in Sec. III C, the sampling of initial and final states needs not be the same, and we simply need a map from the final states to their closest symmetry-equivalent initial state. The set of final states ultimately defines the set of scattering events we account for, represented by the scattering probability $P_{\mathbf{k}\mathbf{k}'}$. These quantities have low symmetry since they combine the initial and final states with the phonon that links them. Thus, the final states of the BTE need to cover the full extent of the valleys. Furthermore, one needs to account for the sharp variations of $P_{\mathbf{k}\mathbf{k}'}$ due to the energy selection rules in Eq. 4. We thus use the fine sampling of the pockets \mathcal{F} for the final states in the BTE. This simply means that the EPC eventually needs to be interpolated on this grid. The set of momenta \mathcal{I} is where we want to compute the scattering times by solving the BTE, and it is convenient to note that the scattering

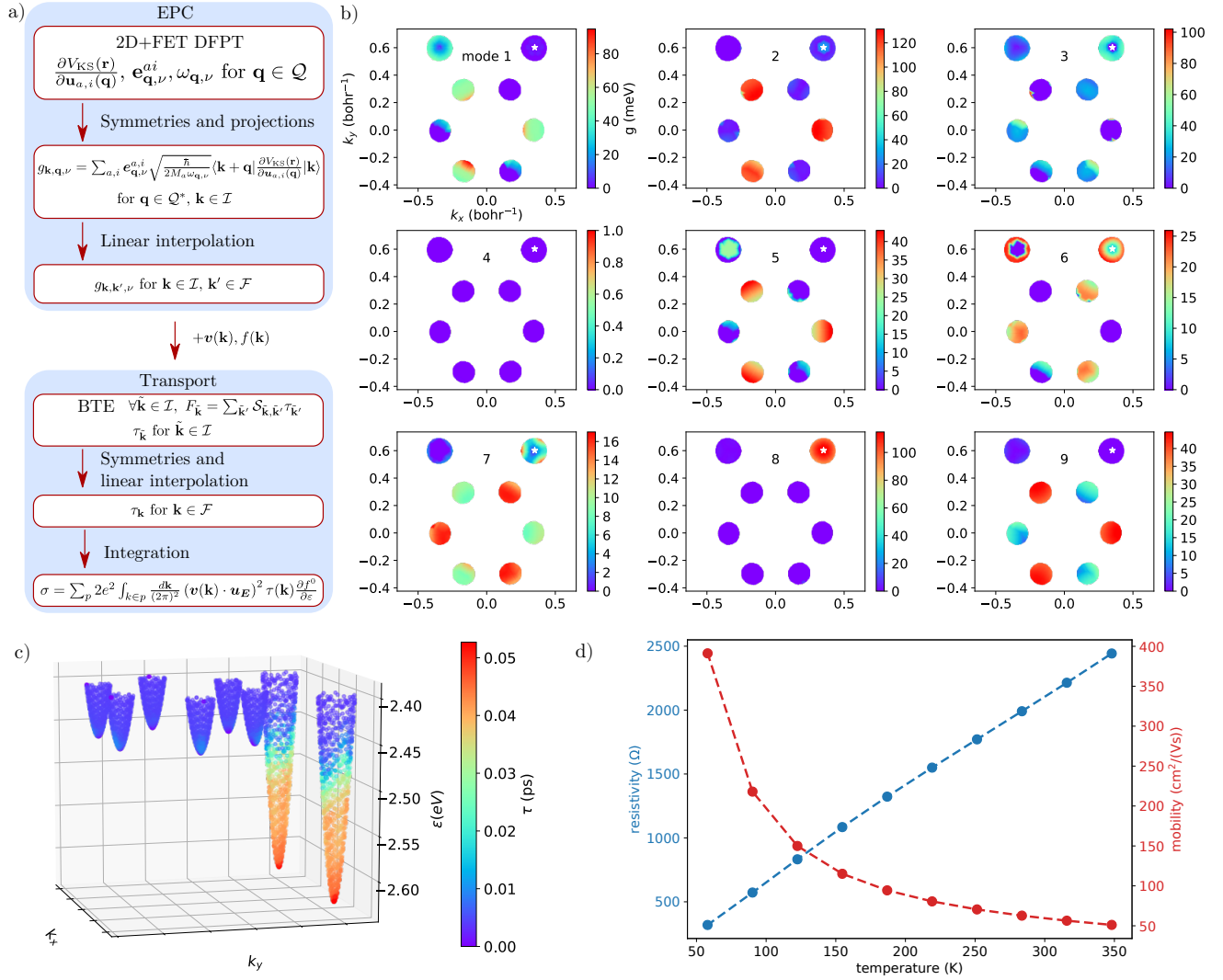


FIG. 1. a) Schematic description of the first-principles workflow for electronic transport b) Interpolated electron-phonon couplings $g_{\mathbf{k},\mathbf{k}'}$ for electron-doped WS_2 . The initial state \mathbf{k} considered here is indicated by a white star; the other points are the possible final states in the finely sampled pockets, where the color of the point indicates the strength of the electron-phonon coupling matrix element. The index of the phonon mode indicated at the top of each subplot refers to a purely energetic ordering of the phonon modes associated with each transition. This implies that crossings in phonon dispersions may lead to discontinuities in the plots. This explains the set of seemingly out-of-place EPC matrix elements in the K' valley for modes 5 and 6, and in lesser measure in the Q valleys for modes 2 and 3. c) Scattering times interpolated on the fine grid of electronic states \mathcal{F} , shown using a color scale for each electronic state in the valleys of WS_2 . d) Temperature-dependent resistivity and mobility of electron-doped WS_2 ($n = 5 \cdot 10^{13} \text{ cm}^{-2}$).

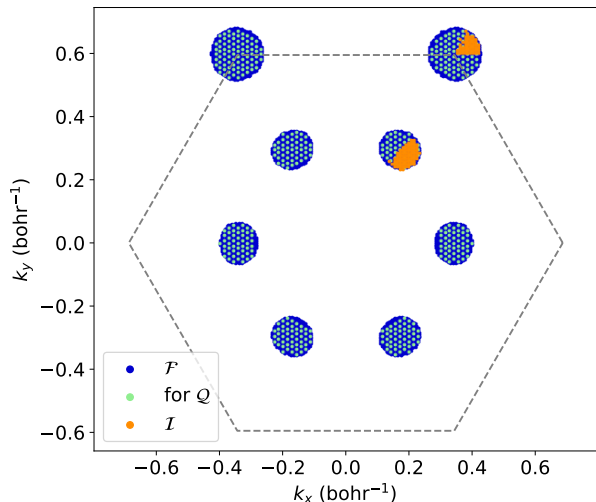


FIG. 2. Representation of the different sampling grids. \mathcal{F} is the fine grid used for the final integration of the conductivity and the sum over final states in the BTE. \mathcal{I} is a coarser grid of irreducible states on which we solve the BTE and compute the scattering times. The grid \mathcal{Q} of phonon momenta on which the linear response is computed is obtained by finding the irreducible set of momenta linking the electronic states from an even coarser grid, represented here in lime green.

times $\tau(\mathbf{k})$ have the symmetry of the electronic eigenenergies $\varepsilon_{\mathbf{k}}$. This is not obvious because the computation of the resistivity involves the electric field and phonons which break the symmetries of the band structure. The integrand in Eq. 10, for example, has the symmetry of the band structure plus the electric field. This quantity and the aforementioned $P_{\mathbf{k}\mathbf{k}'}$ have thus lower symmetry than the electronic states. On the other hand, the form of the ansatz for the perturbed distribution (Eqs. 7 and 8) is such that the effect of the electric field is separated out and $\tau(\mathbf{k})$ essentially represents the dependency of the perturbed distribution on the electronic states only. Further analysis of the BTE (Eq. 9) shows that $\tau(\mathbf{k})$ depends on a sum over all possible final states. While each term of the sum might not have the symmetries of the band structure ($P_{\mathbf{k}\mathbf{k}'}$, e.g., does not), the sum is invariant under the symmetry transformations associated with the BZ. So, since $\tau(\mathbf{k})$ has the symmetry of the band structure, the initial states \mathcal{I} are sampled from an irreducible representation of the valleys. This sampling should be chosen fine enough to capture the variations of the scattering time; however, the size of \mathcal{I} defines the size of the linear system to solve for the BTE and it is a factor in the total number of EPC matrix elements to compute. Those calculations have a non-negligible computational cost, and using the irreducible states in the fine grid of the pockets would be unnecessarily expensive. As shown in Fig. 2, we use a coarser grid: for all materials in this work we found that a grid with a k-points spacing approximately 2.6 times larger than the fine grid \mathcal{F} leads

to a converged solution to the Boltzmann transport equation at a reasonable computational cost. For example, in WS₂, this leads to 126 irreducible initial states, while using the fine pockets grid would have led to more than 800 initial states.

The electronic wave functions in Eq. 5 can be easily recomputed from the ground-state charge density, while the rest is associated with a given phonon perturbation, and is the bottleneck in terms of computational cost (in particular the calculation of $\frac{\partial V_{\text{KS}}(\mathbf{r})}{\partial \mathbf{u}_{a,i}(\mathbf{q})}$). There are methods^{32,33,35,36} to interpolate the perturbation $\frac{\partial V_{\text{KS}}(\mathbf{r})}{\partial \mathbf{u}_{a,i}(\mathbf{q})}$ to the Kohn-Sham potential, but the spirit of the current approach is to compute this quantity directly in DFPT. We will, however, take full advantage of symmetries and use a reasonable sampling of phonon momenta. Each scattering event from an initial to a final states defines a phonon momentum $\mathbf{q} = \mathbf{k}_F - \mathbf{k}_I$, where \mathbf{k}_F spans the pockets $\{\alpha\}$, and \mathbf{k}_I spans the irreducible states in the pockets. We use the same support as for \mathcal{I} and \mathcal{F} , but define a coarser grid, as shown in Fig. 2. We then obtain the set of phonons momenta \mathcal{Q} , where we actually compute the linear response to the phonon perturbation, by the following process: first, we find all possible \mathbf{q} vectors connecting all final states and initial states in the coarse grid. For these, there are many duplicates, since a single momentum can link several pairs of initial and final states, and so we remove those duplicates. The \mathbf{q} points are then reduced by symmetry. Indeed, from one \mathbf{q} -point, the linear response code (as implemented in Quantum ESPRESSO) allows, as a post-process, the computation of $\frac{\partial V_{\text{KS}}(\mathbf{r})}{\partial \mathbf{u}_{a,i}(\mathbf{q}^*)}$ for all \mathbf{q}^* points in the set \mathcal{Q}^* defined as all $\mathbf{q}^* = S(\mathbf{q})$ where S is a symmetry operation of the crystal. The symmetry reduction is done with a tolerance of about the grid step, since the momenta in \mathcal{Q}^* do not always fall exactly on the grid. The number of phonons to compute thus depends on the initial grid chosen for the electronic states in a non-straightforward way. We go through the above process several times until we reach a number of phonons that is largely sufficient to capture the variations of EPC while staying reasonable in terms of computational cost. For example, in WS₂, this results in 200 q-points where to compute the linear response $\frac{\partial V_{\text{KS}}(\mathbf{r})}{\partial \mathbf{u}_{a,i}(\mathbf{q})}$. For materials with less valleys (such as phosphorene studied in Section IV), less than 100 phonons are needed.

In Fig 3 we show both the set of irreducible phonon momenta \mathcal{Q} and the relevant phonon momenta in \mathcal{Q}^* that lead to final states in the BZ for at least one of the initial states.

B. Phonons and EPC calculations

Phonons are computed using the recent implementation of DFPT for gated 2D heterostructures²⁹ in Quantum ESPRESSO^{87,88} (QE). This development includes two important modifications: i) a cutoff of the Coulomb

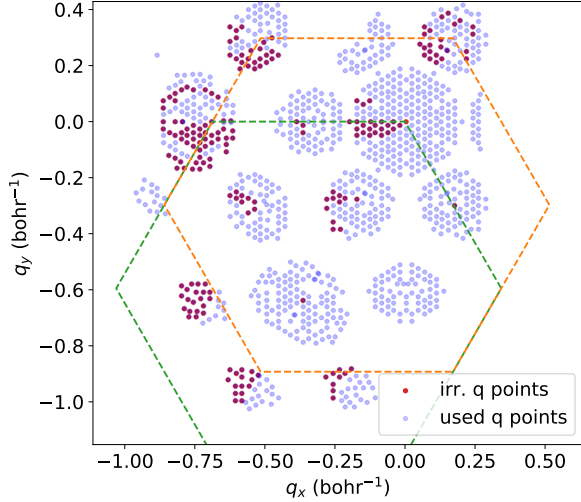


FIG. 3. Irreducible phonon momenta $\mathbf{q} \in \mathcal{Q}$ (in red, those actually computed via DFPT), and all relevant phonons (in light blue) that can be obtained from the latter by symmetry transformations. To help visualizing the corresponding pairs of initial and final electronic states, the dashed lines correspond to a BZ centered either the high-symmetry K point (green) or the bottom of the Q valley (orange) at the origin, the Q valley being approximately halfway between Γ and Q.

interactions in the non-periodic direction^{89,90} and ii) the inclusion of gates to simulate charging of the material in a field-effect setup (FET). The cutoff is necessary to properly account for dimensionality effects^{25,28}: as QE relies on 3D periodic-boundary conditions, there would always be artificial periodic images of the 2D system, and the Coulomb cutoff suppresses spurious interactions between them. The FET setup allows the simulation of the charging of the material in an electrostatic environment that aims to be more realistic than the standard approach of introducing a compensating background of charge uniformly distributed over the full simulation cell (vacuum included). So, we compute the linear response to the phonon perturbations $\frac{\partial V_{\text{KS}}(\mathbf{r})}{\partial \mathbf{u}_{a,i}(\mathbf{q})}$ and the dynamical matrices for $\mathbf{q} \in \mathcal{Q}$ using these two unique features.

These quantities are obtained for all \mathbf{q} in \mathcal{Q}^* by applying symmetry transformations. Then, we compute the EPC matrix elements in Eq. 5 for the $|\mathbf{k}\rangle$ states that are in the irreducible initial states \mathcal{I} . This process is automatized via the AiiDA materials' informatics infrastructure⁹¹ to manage the calculations and store the data. Each symmetry transformation of $\frac{\partial V_{\text{KS}}(\mathbf{r})}{\partial \mathbf{u}_{a,i}(\mathbf{q})}$ and its application to the initial states represents a relatively fast run of the Phonon code of QE. Thanks to AiiDA, such operations can be performed in a highly parallelized fashion. For each initial state, a list of the \mathbf{q} vectors and the corresponding values of $g_{\mathbf{k},\mathbf{k}+\mathbf{q},\nu}$ for each mode is stored; the $g_{\mathbf{k},\mathbf{k}+\mathbf{q},\nu}$ are then interpolated linearly to obtain $g_{\mathbf{k},\mathbf{k}',\nu}$ for \mathbf{k}' on the finer grid of the pockets \mathcal{F} . Fig. 1b) shows

the result of this procedure for electron-doped WS_2 . The data storage and provenance provided by AiiDA ensure that all the information collected from the computationally demanding phonon calculations is safely kept and easily re-used for multiple applications (e.g. one can study phonon-mediated superconductivity starting from the same electron-phonon matrix elements).

C. Transport

Suppose sampling \mathcal{I} yields N_i irreducible initial states, while sampling \mathcal{F} yields N_f final states. Writing the BTE for the irreducible states yields N_i equations relating $\tau(\tilde{\mathbf{k}})$ for $\tilde{\mathbf{k}} \in \mathcal{I}$ to $\tau(\mathbf{k}')$ for N_f $\mathbf{k}' \in \mathcal{F}$.

$$\forall \tilde{\mathbf{k}} \in \mathcal{I},$$

$$\begin{aligned} \tau(\tilde{\mathbf{k}}) \times \sum_{\mathbf{k}'} P_{\tilde{\mathbf{k}}\mathbf{k}'} (1 - f^0(\mathbf{k}')) \mathbf{v}(\tilde{\mathbf{k}}) \cdot \mathbf{u}_E = \\ (1 - f^0(\tilde{\mathbf{k}})) \mathbf{v}(\tilde{\mathbf{k}}) \cdot \mathbf{u}_E \\ + \sum_{\mathbf{k}'} P_{\tilde{\mathbf{k}}\mathbf{k}'} (1 - f^0(\mathbf{k}')) (\mathbf{v}(\mathbf{k}') \cdot \mathbf{u}_E) \tau(\mathbf{k}'). \end{aligned} \quad (11)$$

This system can be solved iteratively, using the the closed-form solution in I as a starting point. Each iteration gives us the values of τ for $\mathbf{k} \in \mathcal{I}$ grid. It is then rotated according to the symmetries of the band structure, interpolated linearly on the fine grid of the pockets $\mathbf{k}' \in \mathcal{F}$, and put back into the next cycle, until self-consistency.

We address below a couple of technical issues that prove important if one wants to have an accurate and robust numerical solution. To arrive at the final form of the BTE, we address the fact that its solution $\tau(\mathbf{k})$ is ill-defined when $\mathbf{v}(\tilde{\mathbf{k}}) \cdot \mathbf{u}_E$ approaches zero. Indeed, considering $\mathbf{v}(\tilde{\mathbf{k}}) \cdot \mathbf{u}_E = 0$, any $\tau(\tilde{\mathbf{k}})$ satisfies Eq. 11. In practice, this brings numerical noise. This situation can happen: i) if $\mathbf{v}(\tilde{\mathbf{k}}) \approx 0$, which is relatively rare in practice (e.g. only when $\tilde{\mathbf{k}}$ is very close to the extremum of a valley); ii) if $\mathbf{v}(\tilde{\mathbf{k}}) \perp \mathbf{u}_E$, where \mathbf{u}_E is the direction of the electric field. Situation i) can be treated approximately, without much consequences on the transport results (indeed, states with zero velocity do not contribute to transport), and we compute the scattering time using the closed form of the BTE reported in the App. I. In situation ii), we do need a consistent evaluation of $\tau(\mathbf{k})$. Indeed, even though $\tilde{\mathbf{k}} \in \mathcal{I}$ does not contribute to the conductivity because its velocity is perpendicular to the field, this is not necessarily true for all $\mathbf{k} \in \mathcal{F}$ that are equivalent to $\tilde{\mathbf{k}}$ according to the symmetries of the BZ. We thus use the following technique: since $\tau(\tilde{\mathbf{k}})$ has the symmetry of the band structure, it does not depend on the direction of the electric field. In other words, any choice for the direction of the electric field gives the same τ 's. Thus, we are free to use any direction for the electric field to solve the BTE, and we can choose different directions for each

of the N_i equations corresponding to the N_i $\tilde{\mathbf{k}}$ points. For each $\tilde{\mathbf{k}}$, we choose the direction $\mathbf{u}_{\tilde{\mathbf{k}}} = \frac{\tilde{\mathbf{k}}}{|\tilde{\mathbf{k}}|}$, where $\tilde{\mathbf{k}}$ is $\tilde{\mathbf{k}}$ taken from the extremum of its valley, since $\mathbf{v}(\tilde{\mathbf{k}}) \perp \mathbf{u}_{\tilde{\mathbf{k}}}$ virtually never happens.

We then have a well-behaved set of equations. The other numerical issue is the treatment of the δ functions in Eq. 4. The standard numerical procedure is to replace them by Gaussian functions and test the convergence of the solution with respect to the corresponding broadening. However, convergence is very slow, and even with the relatively fine grids used for here, the corresponding errors on the mobilities can reach a few percents. In addition, the automation of these convergence tests can be challenging. An alternative is to use more sophisticated integration techniques like the so-called triangles method^{61,62} (two-dimensional equivalent of the tetrahedron method⁹²), which amounts to performing the sum analytically as an integral by interpolating the functions involved linearly within three points that form a triangle. Although slower, it gives more accurate results and this is what we implemented here. To the best of our knowledge, it is the first application of this method to the BTE. As a final remark, note that an iterative procedure is not needed in principle. The above system of equations can be solved algebraically. As discussed in App. II, however, the use of Gaussians and the associated choice of broadening parameter becomes necessary.

Once we have the angular and energy dependent $\tau(\mathbf{k})$, which does not depend on the electric field in itself, we can compute the conduction integral for an arbitrary direction of the electric field, thus probing any diagonal element of the conductivity tensor.

IV. RESULTS

We have applied our approach to a set of six different cases: five electron-doped materials (WS₂, MoS₂, WSe₂, arsenene, and phosphorene), as well as hole-doped phosphorene. These are common 2D systems often praised for their potential for transport applications. Also, this set leads to an interesting diversity of band structures, in terms of valleys, their symmetries and their energetic accessibility. Let us stress that we are working here in the framework of DFT, rather than higher levels of theory, and without spin-orbit coupling (SOC). Both approximations can of course affect the bands of the materials studied here and have an impact on mobility^{49,55}. In particular, inclusion of many-body corrections within, e.g., the GW approximation, would not only correct quasiparticle energies of the pristine, undoped materials, but would also improve the description of band renormalization effects associated with free carriers, especially at high doping. For SOC, we expect the variations to be relatively small for electron-doped arsenene and phosphorene⁷⁶. The case of TMDs is a more delicate one: the relative positions of the K and Q valleys seems to be sensitive to many aspects of the calculations, like the inclusion

of SOC⁹³, choice of pseudo potentials, lattice parameters, level of theory⁹⁴ (DFT versus GW) or doping⁹³. Thus, while we will be able to compare between the three TMDs and discuss qualitative trends, we do not claim to be quantitative with respect to experiments. That being said, the methodological approach presented in this work is very flexible. One can combine the electron-phonon coupling matrix elements found in DFPT with the band structure found by any mean; e.g., one can use a band structure computed at the highest level of theory, and/or correct it to better fit experiments, before inserting it in the workflow. Regarding SOC, it can be easily included in the band structure calculations and EPC calculations; further development is planned to include it in the solution to the BTE.

Another important approximation we make, common to most DFT/DFPT approaches to compute phonons and EPC from first principles¹⁷, is the adiabatic approximation. This means that electrons are assumed to be able to relax to their ground state during phonon perturbations, either as a result of their motion being faster than phonon oscillations (Fermi velocity higher than the phonon phase velocity) or because the electronic scattering times due to other momentum-changing sources of disorder are short enough to establish equilibrium^{95,96}. This amounts to taking the zero-frequency limit – allowing intraband transitions – in the phonon self-energy^{16,17}, which, among other things, results in discarding non-adiabatic screening effects⁹⁷. The former approximation can sometimes break down, especially in metals, as is the case for the non-adiabatic Kohn anomalies in graphene^{98,99}. Although these effects can be predicted from first principles^{33,96,98}, even accounting for correlations beyond DFT¹⁰⁰, their inclusion in the solution of the BTE has never been performed in first-principles approaches and will not be considered here. Dynamical screening of electron-phonon interactions seems even more challenging, and it's typically overlooked in first-principles investigations¹⁷ or at most introduced via model dielectric functions¹⁰¹.

In the calculations, we chose an electrostatic doping of $5 \times 10^{13} \text{ cm}^{-2}$. While undoubtedly high, this doping is experimentally achievable, at least with the use of ionic liquid gates^{1,102}. In addition, this regime is interesting from a fundamental point of view, because it allows to suppress extrinsic contributions, like charge impurities via screening, thus getting closer experimentally to phonon-limited transport. This high doping regime is poorly studied from first principles, and accessible thanks to our implementation of DFPT for gated materials without any analytical corrections. Nonetheless, it also poses some additional challenges, such as the emergence of band-renormalization effects, electron-electron and electron-plasmon scattering, which has been posited to be relevant at high doping^{103,104}; these are beyond the scope of the present manuscript. As far as applications are concerned, the relevant doping regime varies. High doping is relevant for several possible application,

such as high frequency electronics. For logic-gate transistors operating at very low densities, the zero doping limit is more relevant. The method presented here could be applied also in this case, but we chose to propose a new perspective with respect to the theoretical literature already treating this limit. As a consequence, in the following, comparisons with theoretical works in the zero doping limit must be taken carefully. More generally, many devices might operate at moderate doping densities ($\sim 10^{12} \text{ cm}^{-2}$). In this regime, the application of our approach would still be possible, although it would require the use of finer k-point sampling for the phonon calculations, which we chose to avoid here given the number of systems studied. Nevertheless, for moderate doping, the high doping results presented here might be more relevant than undoped results.

As previously mentioned, first-principles calculations are performed with the Quantum ESPRESSO distribution^{87,88} including a 2D Coulomb cutoff and the possibility to charge the material with gates²⁹, and using the SSSP Accuracy (version 0.7) library^{105–108}. Structures are taken from the database described in Ref. 11. To build this database, structural relaxations were performed in the neutral material, using the SSSP library as well and a k-point sampling corresponding to a spacing of 0.2 \AA^{-1} in each direction. We use a symmetric double-gate setup to charge the materials with a density of $5 \times 10^{13} \text{ cm}^{-2}$ electrons or holes for all systems except for electron-doped phosphorene, where we choose a lower density of $5/3 \times 10^{13} \text{ cm}^{-2}$ to avoid raising the Fermi level too high in the conduction band, where additional valleys appear. Each gate carries half the opposite charge of the material, such that the electric field has equal norm but opposite direction on each side of the material. We could also have used a single-gate setup, with an electric field only on one side, but no large difference is expected since the impact of the electric field setup should come mainly from its effect on spin-orbit coupling, which is not included here. Barrier potentials are added to avoid leakage of electrons towards the gates. These also lead to a hardening of the ZA phonons in the long-wavelength limit, with a non-zero frequency at Γ around $10 - 25 \text{ cm}^{-1}$ for the materials considered. This emulates a relatively soft out-of-plane mechanical interaction with gate dielectrics or substrate compared to interlayer interactions in the layered parent 3D material, since breathing ZA modes are usually in the $20\text{-}50 \text{ cm}^{-1}$ range. Ground state and linear-response calculations on the charged materials are performed with a $32 \times 32 \times 1$ k-point grid and 0.02 Ry Methfessel-Paxton smearing to sample the Fermi surface. Note that we are working at relatively high doping, such that the Fermi surface is large enough to be sampled correctly. Non self-consistent calculations are performed to obtain the band structure on the fine grid \mathcal{F} . Band structures and phonon dispersions are reported in the App. III.

The interpolated EPC matrix elements for electron-doped WS_2 are shown in Fig. 1; for electron-doped ar-

senene in Fig. 4; and for hole-doped phosphorene in Fig. 5. Equivalent plots for electron-doped MoS_2 and WSe_2 can be found in the App. IV; they are very similar to WS_2 . The angular dependencies of the EPC are non-trivial: the EPC can undergo some rather sharp variations, most often for intravalley transitions via acoustic modes. For intervalley transitions, we observe overall smoother variations if we ignore the discontinuities coming from phonon crossings. However, intervalley scattering is activated or not depending on the valleys and the mode in rather non-trivial ways. These plots also serve to give a visual confirmation that we use sufficient sampling to capture the variations of the EPC. One important aspect to keep in mind when interpreting these plots and the transport properties of the system is that energy and momentum conservation conditions drastically reduce the final states effectively relevant for a given initial state.

The linearized BTE is solved in all these systems, giving the mobilities shown in Fig. 6. These cover three orders of magnitude, and the hole side of phosphorene shows mobilities ten times larger than the rest, almost reaching $10^3 \text{ cm}^2/\text{Vs}$ at room temperature. For comparison, electron-doped graphene has mobilities on the order of 10^4 to $10^5 \text{ cm}^2/\text{Vs}$ depending on the density. Table I summarizes our findings, focusing on room-temperature results, and compares them with some values available in the literature. To characterize the temperature dependence of mobilities, we report the parameter γ in Table II, defined as $\mu \propto T^{-\gamma}$. Below, we identify the general trends and discuss three important factors in the prediction of transport properties in 2D materials. Finally, we argue that those three factors might account for the discrepancies observed in Table I.

A. Intervalley scattering

The ranking of the above materials in terms of mobility reflects the importance of intervalley scattering. This is clearly demonstrated by considering the three TMDs: these have essentially the same type of electronic and phonon band structures, as well as similar EPC matrix elements. Yet, we obtain an order of magnitude variation in the mobilities. This stems from the position of the Q valley: indeed, as the Q valley approaches the Fermi level, it offers an additional scattering channel for the electrons. As shown in Fig. 7, the scattering time gets shorter (more scattering) at energies close to the bottom of the Q valleys. The largest contributions to the resistivity of TMDs ($\approx 80\%$ ¹²¹) comes from the scattering with the LA and TA modes: LA at Γ (intervalley scattering) and M ($\text{K} \leftrightarrow \text{Q}$ scattering) and TA at K ($\text{K} \leftrightarrow \text{K}'$ scattering). This is not obvious from the plots of the electron-phonon matrix elements, because the dispersions of the three acoustic modes cross each other between Γ and K, and between Γ and Q. However, looking at the phonon displacements, it is quite clear that in-

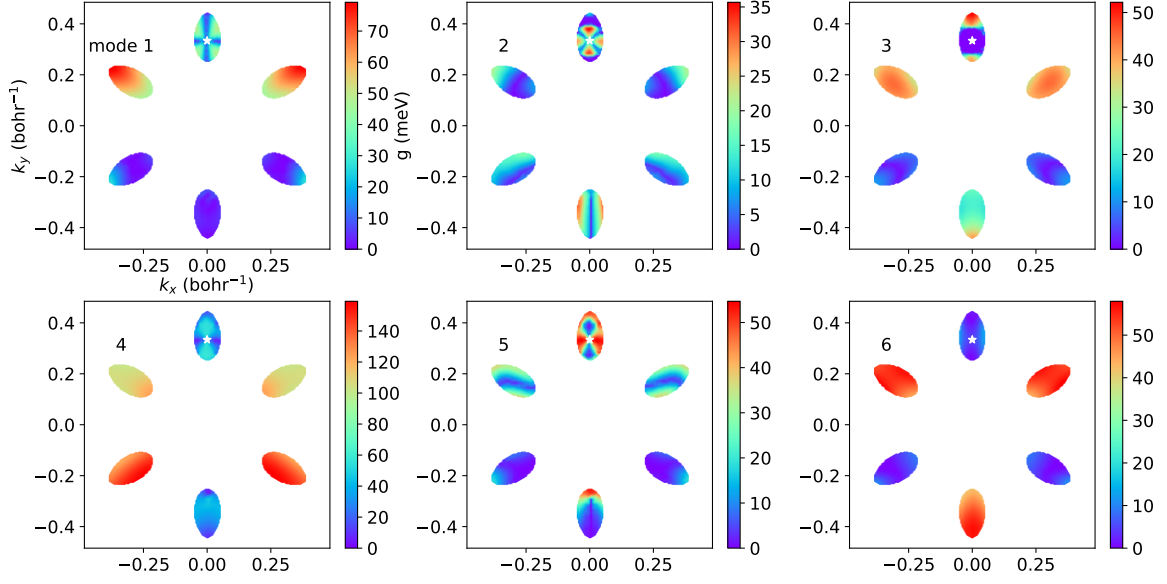


FIG. 4. Interpolated $g_{\mathbf{k}\mathbf{k}'}$ for electron-doped arsenene. The initial state considered is indicated by a white star. The rest of the points are the possible final states in the finely sampled pockets and the color of the point indicates the strength of the electron-phonon coupling matrix element. The index of the phonon mode indicated at the top of each subplot refers to a purely energetic ordering of the phonon modes associated with each transition.

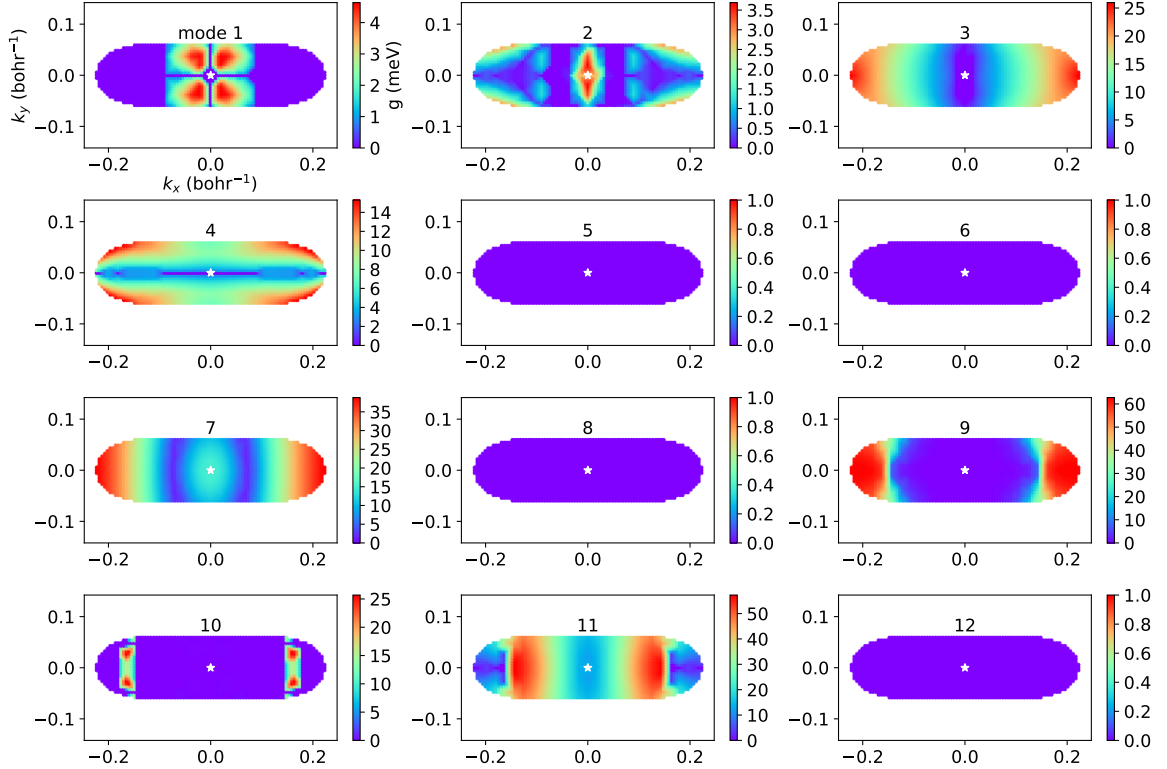


FIG. 5. Interpolated $g_{\mathbf{k}\mathbf{k}'}$ for hole-doped phosphorene. The initial state considered is indicated by a white star. The rest of the points are the possible final states in the finely sampled pockets and the color of the point indicates the strength of the electron-phonon coupling matrix element. The index of the phonon mode indicated at the top of each subplot refers to a purely energetic ordering of the phonon modes associated with each transition.

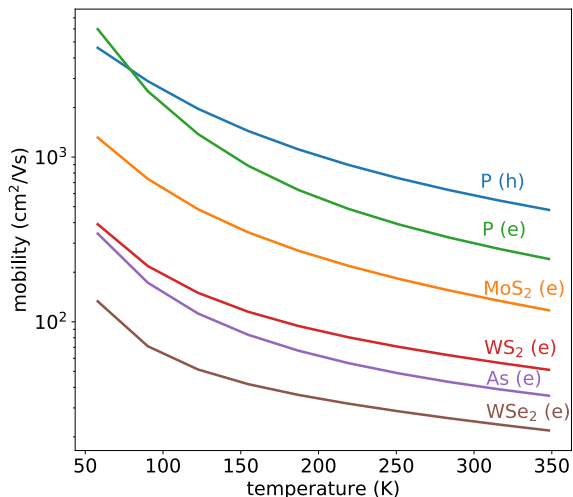


FIG. 6. Mobilities as a function of temperature for electron-doped MoS₂, WS₂, WSe₂, arsenene and phosphorene, as well as for the hole side of phosphorene. The carrier density is $5 \times 10^{13} \text{ cm}^{-2}$ for all systems except electron-doped phosphorene where it is $5/3 \times 10^{13} \text{ cm}^{-2}$.

plane acoustic modes are associated with the regions of strong electron-phonon coupling in the first three subplots of Fig. 1b, and in Figs. A3, A5 and A4 of App. IV.

The multi-valley nature of a material does not necessarily deteriorate the mobility in itself. The presence of multiple valleys increases both the accessible phase space for scattered states and the density of states, and the corresponding effects on the mobility cancel each other. Rather, it is the existence of a strong EPC between the valleys that increases scattering and lowers the mobility. For the small subset studied here, all multi-valley materials showcase strong intervalley EPC. It may be argued, in general, that intervalley EPC is often strong compared to intravalley EPC. This could first be explained by the fact that intervalley EPC is not bound to vanish at long wavelengths, contrary to the coupling to acoustic phonons. Second, it involves larger phonon momenta and the EPC tends to be less screened, since the dielectric function goes to one in the short-wavelength limit.

B. Symmetries of the valleys

Effective masses are among the most influential features to consider when studying mobilities, and anisotropic effective masses can be very beneficial. Indeed, small effective masses have the benefit of bringing large carrier velocities while large effective masses have the benefit of bringing high carrier densities. Thus, one might combine those benefits having a small effective mass in the transport direction and a large one in the perpendicular direction. This contributes to phosphorene's

good transport performance. In fact, phosphorene is the only material in the present study showing significant transport anisotropy. The transport properties of TMDs are isotropic because the bottom of the K and Q valleys are roughly isotropic. In the case of arsenene, each single valley is quite anisotropic, but when summing up the six equivalent valleys the angular dependency of the transport averages out and vanishes⁷⁹. Fig. 8 shows the mobility of P (h), As (e) and WS₂ (e) as a function of the direction of the electric field. The mobility of phosphorene is highly directional, while all others are isotropic.

C. Doping effects on electron-phonon interactions

The effects of doping on electron-phonon scattering are many. The first one is to move the Fermi surface within the electronic landscape. This leads to variations of the density of states and determines whether certain valleys are accessible via phonon scattering or not. As we saw in TMDs, the activation of intervalley scattering can have drastic consequences on transport. Those effects come from the energy selection rules of Eq. 4. Doping also has consequences on the strength of EPC matrix elements themselves (Eq. 5). A well-known and important effect is the additional screening coming from the electrons added in the conduction band or holes in the valence band. In our computational framework, this is inherently accounted for since we compute the linear-response of the charged system. Any EPC related to a periodic variation of the effective scalar potential in which the electrons move will be screened. This includes: i) a variation of the charge state via a variation of the area of the unit cell, as induced by longitudinal acoustic phonons; ii) any EPC related to dipole or Born effective charges, like Fröhlich or piezo-electric EPC, in which phonons interact with electrons via the generation of electric fields; iii) other less straightforward mechanisms, like the gate-induced coupling to flexural phonons in graphene^{29,75}. In general, considering only the above types of EPC is largely insufficient in doped materials, as electronic screening strongly reduces their contribution, and bare interactions or weakly screened intervalley couplings dominate.

Doping also affects EPC beyond screening: as the occupations of the valleys vary, certain orbitals/bands in the material get populated or depleted, which can directly change the amplitude of the coupling. This happens in TMDs, as shown in Fig. 9 in which we computed intravalley scattering for several doping levels. In particular, we compute the average of the long-wavelength coupling $\langle g^2 \rangle$ along a fixed iso-energetic line at $\varepsilon = E$, by taking a few initial states on the iso-energetic section of each the K and Q valleys, and six phonon momenta with a fixed small norm. Linear-response calculations are then performed for each doping to capture non-trivial dependencies of the EPC matrix elements. We average on the

TABLE I. Room-temperature mobilities of the 6 systems considered (at the DFT/DFPT level without SOC). Mobilities are given in cm^2/Vs , doping densities are indicated in parentheses, in units of 10^{13} cm^{-2} . Question marks for densities of experimental works indicate that the information was not provided. For theoretical works, "0" means that the mobility was derived in the zero doping limit (this includes calculations based on the density-independent formulae). Note that SOC is not included in any of those works. Results on phosphorene are reported in both the armchair (ac) and zig-zag (zz) directions.

Material (e or h doped)	Present result $\mu(n)$	Other first-principles results $\mu(n)$	Experimental $\mu(n)$
MoS ₂ (e)	144 (5)	265 (5) ²⁴ , 150 (0) ⁵⁴ , 130 (0) ¹⁰⁹ , 320 (0.01) ⁵³ , 410(0.01)-340(1) ⁵² , 340 (0) ¹¹⁰	217 (0.46) ² , 150 (0.7) ¹¹¹ , 81 (0.7) ¹¹² , 63 (1.35) ¹¹³ ,
WS ₂ (e)	60 (5)	320 (0) ⁴² , 1103 (0) ¹¹⁰	44 (10) ¹¹⁴ , 44 (?) ¹¹⁵ , 45 (0.6) ¹¹⁶ , 25-83 (0.7) ¹¹⁷ , 214 (?) ¹¹⁸
WSe ₂ (e)	25 (5)	30 (0) ⁴² , 705 (0) ¹¹⁰	7 (0) ¹¹⁹ , 30 (1-1.5?) ¹²⁰
As (e)	41 (5)	21 (-) ⁸⁰ , 1700 (0) ⁷⁹	-
P (h-ac)	586 (5)	640-700 (0) ⁷⁶ , 460 (0) ⁴⁵ , 292 (5) ⁴⁶ , 140 (1) ⁷⁷ , 19 (0) ⁴⁸	
P (h-zz)	44 (5)	10000-26000 (0) ⁷⁶ , 90 (0) ⁴⁵ , 157 (5) ⁴⁶ , 15 (1) ⁷⁷ , 3 (0) ⁴⁸	
P (e-ac)	302 (5/3)	1100-1140 (0) ⁷⁶ , 210 (0) ⁴⁵ , 738 (5) ⁴⁶ , 430 (5) ⁴⁷ , 140 (1) ⁷⁷ , 20 (0) ⁴⁸	
P (e-zz)	35 (5/3)	80 (0) ⁷⁶ , 40 (0) ⁴⁵ , 114 (5) ⁴⁶ , 80 (5) ⁴⁷ , 25 (1) ⁷⁷ , 10 (0) ⁴⁸	

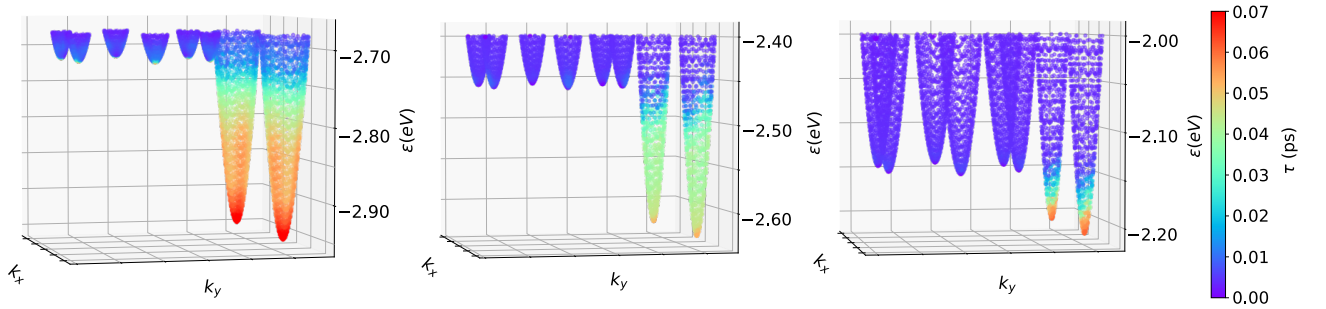


FIG. 7. Scattering times in MoS₂, WS₂, and WSe₂ (from left to right). The color scale is the same for all subplots. The scattering rate (\hbar/τ) clearly increases for states with energy high enough for the Q valley to be accessible. The Fermi levels are : -2.83 , -2.46 , and -2.13 eV, respectively.

TABLE II. Temperature dependence of the mobility, represented by the factor γ such that $\mu \propto T^{-\gamma}$.

Material (e or h doped)	γ ($T \leq 150$ K)	γ ($T > 150$ K)
MoS2(e)	1.33	1.34
WS2(e)	1.28	0.99
WSe2(e)	1.28	0.79
As(e)	1.49	1.04
P (h-ac)	1.14	1.36
P (e-ac)	1.96	1.60

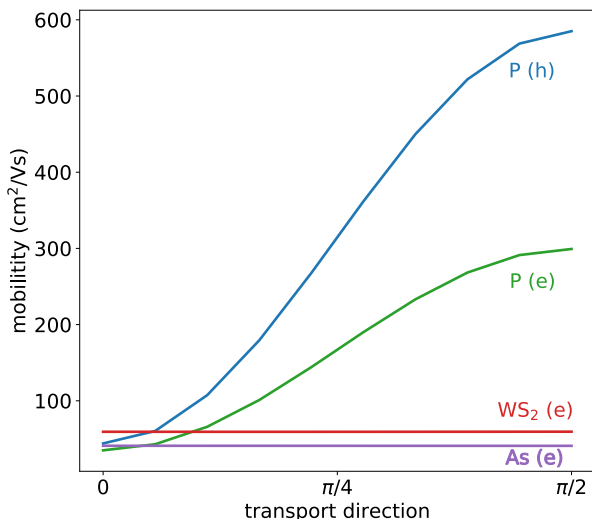


FIG. 8. Angle-dependent mobilities at room temperature for hole-doped and electron-doped phosphorene, and electron-doped arsenene and WS₂. The angle corresponding to the transport direction refers to the direction of the in-plane electric field driving the current with respect to the \mathbf{x} direction indicated in the plots of EPC. For phosphorene, 0 ($\pi/2$) corresponds to the zig-zag (armchair) direction. While phosphorene shows highly anisotropic transport, only very small variations ($\approx 10^{-2}$ cm²/(Vs), below numerical accuracy) can be observed in WS₂ and arsenene.

phonon momenta and on the initial states to get $\langle g_\alpha^2 \rangle$ for each valley $\alpha = K, Q$. We sum the contributions from acoustic and optical phonon modes separately. Fig. 9 shows that as doping increases in WS₂, the intravalley coupling in K increases while it decreases in Q. The couplings to both acoustic and optical phonons show variations of 50 ~ 60%. Similar trends were observed in the literature¹²², but this kind of effect is poorly understood and difficult to predict, highlighting the importance of explicitly including doping in the linear-response calculations.

We note that the way doping is induced can be important. An example is the gate-induced coupling to flexural phonons in graphene^{29,75}, related to a broken mirror symmetry with respect to the graphene plane. However, we do not expect such effects to be significant for the subset of materials studied here.

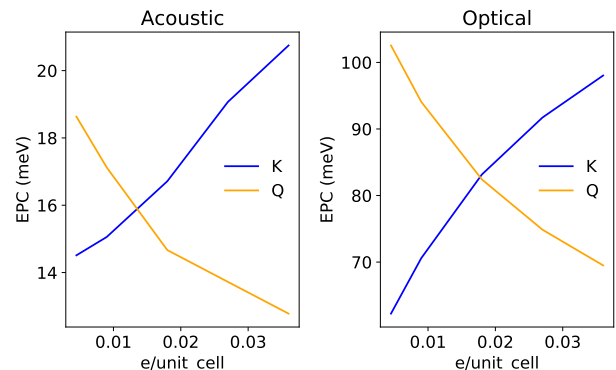


FIG. 9. Doping dependency of intravalley scattering in both electron valleys of WS₂. The EPC is measured by the quantity $\langle g_\alpha^2 \rangle$, described in the text.

Last, we mention that doping obviously leads to a finite density of free carriers. This can give rise to additional loss mechanisms such as electron-electron and electron-plasmon scattering, which can in principle affect the transport properties of a material^{103,104} but are not included here.

D. Comparison with literature

We first discuss the comparison with the other theoretical works reported in Table I. Due to the diversity of the techniques employed, both at the BTE and EPC level, discrepancies between different first-principles results can have many different explanations. However, comparison with the literature points to the three factors discussed above being quite relevant. Indeed, intervalley scattering, doping and anisotropy, which we identified to be essential in determining the transport properties of 2D materials, also turn out to be treated quite differently in different works.

First and foremost, let us note that in general the mobility $\mu = \sigma/n$ depends strongly on carrier density n . In the context of doped semiconductors, the conductivity σ tends to increase (or possibly decrease in more peculiar cases, like TMDs, where intervalley scattering can be activated above a certain doping) rather slowly as a function of n , so the mobility tends to decrease. Thus, direct comparison of mobilities calculated or measured at different carrier densities has limited meaning. One must keep in mind that in the small doping limit, the mobility might be increased by a factor 3 ~ 5 with respect to the present high-doping results. In the references mentioned in Table I, first-principles calculations are done in neutral materials. The calculated mobilities marked by a "0" in Table I apply to the undoped limit, as clearly stated in the references using Boltzmann transport^{48,54}, and implied in references based on Monte-Carlo transport^{42,45,109}, and Takagi's formula^{76,79,80,110,123}. For those works, the com-

parison with the high-doping mobilities presented here should be taken with caution. We report them nonetheless to highlight the importance of doping and the ambiguity surrounding it, given that those values are sometimes compared with experimental measurements at finite doping. For the theoretical works where a finite carrier density is indicated, doping is sometimes included only a posteriori as a shift of the Fermi level in the computation of transport properties. In some instances, analytical models of screening are used, but those are not well established in 2D materials. In any case, we have seen that the effect of doping goes beyond shifting the Fermi level and electronic screening. Thus, performing EPC calculations with doping explicitly included is important to evaluate the transport properties of doped materials. This appears to be particularly important in phosphorene, where we find a larger mobility compared to most of the results in literature^{45,46,48,77}. In particular we find that, due to the doping induced screening, the LA mode is less effective in scattering electrons than what previously reported and only contributes for approximately 50% of the total scattering processes. Screening effects might be large enough to compensate the $1/n$ dependency of the mobility and the small doping mobility could be smaller or of the same order of magnitude as the high doping mobility.

Many models include intravalley coupling only (e.g. “deformation potential” models), thus neglecting intervalley transitions. Furthermore, given the complexity of EPC in multivalley materials, most analytical models of EPC with fitted parameters from first-principles are likely to be incomplete. It is no coincidence that works employing such approaches show the greatest differences with the current results (even assuming a factor 10 increase of the mobility with respect to our result in the low doping limit), often largely overestimating mobility, like the results on TMDs reported in Ref. 110 or on arsenene in Ref. 79. When intervalley scattering is accounted for, it can still be a source of discrepancy depending on the relative positions of the valleys. This is similar to what happens in GaAs, where the value of mobility at high-temperature crucially depends on the relative energy between the Γ and L valley^{55,124,125}. In 2D, this is relevant for TMDs, in which the position of the Q valley with respect to the bottom of the K valley is difficult to determine, as mentioned before, from first-principles. For example, the energy separation between the two extrema in MoS₂ ranges between 70¹⁰⁹ and 260 meV^{52,54} with the latter results closer to our calculations. This difference brings a large intervalley contribution for MoS₂ in Ref. 109 that we don’t observe, and that we find instead in the W-based TMDs. The relative energy separation of the K and Q valley affects also our ranking in terms of electron mobility among the TMDs, with MoS₂ performing better than WS₂, contrary to the findings in Ref. 42. In Ref. 42 the energy separation between K and Q is 80 meV in MoS₂ and 67 meV in WS₂ resulting in a similar intervalley scattering between the two materials

and a better mobility for WS₂ on the basis of its lighter effective mass. In our case instead the K-Q energy separation shows a larger variation, from 257 meV in MoS₂ to only 178 meV in WS₂ resulting in an increased intervalley scattering that undermines the advantage of a lighter effective mass.

The anisotropy of the valleys affects the validity of approximated solutions to the Boltzmann transport equation. In particular, for anisotropic phosphorene, the energy relaxation time approximation (see App. I) gives results with up to 30% errors with respect to the full solution. For the other materials studied here, with isotropic transport properties, this error reduces to a few percents. Although these errors can be acceptable in most cases, a full solution to the BTE beyond the relaxation-time approximation is valuable for quantitative comparison with experiments. In any case, given that the errors associated to different approximate solutions to the BTE are not obvious to determine a priori, and that the numerical solution to the full linearized BTE is comparable in terms of computational cost, we consider it a useful in general.

We now discuss the comparison with experimental work, which concerns only the TMDs reported in Table I. As already discussed, the positions of the valleys with respect to the Fermi level play a very important role, and since our bands are computed within DFT without SOC, we do not claim quantitative agreement with experiments. In practice, one could measure both higher or lower mobilities. For example, one could measure a lower mobility if the Q valley is lower, and a higher one if spin conservation restricts available scattered states. Nevertheless, experimental mobilities for TMDs are relatively close to our predictions, whereas one would expect additional extrinsic scattering processes to give significantly lower values. This can be explained in several ways. First, since mobility goes as $1/n$ and intervalley scattering is activated as the Fermi level increases and crosses more valleys, we can expect the high-density intrinsic mobilities computed here to be lower than experiments performed at lower densities. Second, one could conclude that the importance of extrinsic contributions, like remote phonons, might have been overestimated in the past. Conversely, extrinsic mechanisms leading to an enhanced mobility, such as the phonon mode quenching mentioned in Ref. 113, could be more effective than expected. Undoubtedly, the complexity of electron and phonon dynamics in TMDs calls for further work before reaching numerical agreement between simulations and experimental measurements.

V. CONCLUSIONS

We have developed an automated procedure to determine the transport properties of 2D materials from first-principles. We aim for the highest accuracy achievable within the framework of density-functional pertur-

bation theory, with as few assumptions and simplifications as possible. The method includes several strengths and improvements with respect to existing approaches. Electron-phonon coupling matrix elements are directly computed from density functional-perturbation theory in the correct dimensionality framework and with the correct electrostatics of field-effect doping. The linearized Boltzmann transport equation is solved numerically in full, beyond relaxation-time approximation or any other closed-form expressions for the scattering time. The implementation of this entire transport workflow within the AiiDA infrastructure provides great flexibility to improve or adapt the method to different applications, as well as the data storage and provenance necessary to build and disseminate databases. Here, we studied in detail a small test set of six systems (electron-doped MoS₂, WS₂, WSe₂, arsenene and phosphorene as well as hole-doped phosphorene) presenting different characteristics. Our results point out the crucial role of intervalley scattering, band anisotropy and doping to the transport properties of 2D materials, in turn underscoring the importance of an accurate treatment of these aspects in first-principles simulations. Hole-doped phosphorene is found to yield the highest mobility, thanks to its mono-valley and anisotropic nature. Electron-doped arsenene shows a

lower mobility than could be expected, due to the importance of intervalley scattering. The transport properties of electron-doped TMDs are found to be very sensitive to the relative positions of the K and Q valleys: these quantities are still subject of study at the highest levels of theory and experimentally. While this work is based on DFT band structures, more accurate predictions would be reached by including spin-orbit interactions, GW corrections and by fitting at least the most important features of the valleys to experimental data.

ACKNOWLEDGEMENTS:

This work has been in part supported by NCCR MARVEL (N.M. and D.C.). Calculations were performed on the Marconi - KNL supercomputer in Cineca under PRACE project PRA15.3963. D.C. acknowledges support from the EPFL Fellows fellowship programme cofunded by Marie Skłodowska-Curie, Horizon 2020 grant agreement no. 665667. M.G. acknowledges support from the Swiss National Science Foundation through the Ambizione career programme.

APPENDIX

I. CLOSED FORM OF BTE

Re-writing Eq. 9 as

$$1 = \sum_{\mathbf{k}'} P_{\mathbf{k}\mathbf{k}'} \frac{1 - f^0(\mathbf{k}')}{1 - f^0(\mathbf{k})} \times \left\{ \tau(\mathbf{k}) - \tau(\mathbf{k}') \frac{\mathbf{v}(\mathbf{k}') \cdot \mathbf{u}_E}{\mathbf{v}(\mathbf{k}) \cdot \mathbf{u}_E} \right\}, \quad (\text{A1})$$

we see that a closed form can be obtained by assuming $\tau(\mathbf{k}) \approx \tau(\mathbf{k}')$:

$$\frac{1}{\tau(\mathbf{k})} = \sum_{\mathbf{k}'} P_{\mathbf{k}\mathbf{k}'} \frac{1 - f^0(\mathbf{k}')}{1 - f^0(\mathbf{k})} \times \left\{ 1 - \frac{\mathbf{v}(\mathbf{k}') \cdot \mathbf{u}_E}{\mathbf{v}(\mathbf{k}) \cdot \mathbf{u}_E} \right\}, \quad (\text{A2})$$

To obtain the closed form used in this work to initialize the iterative solution to the BTE, we replace \mathbf{u}_E by the direction of \mathbf{k} with respect to the bottom of the corresponding valley, as explained in the main text. One may also replace \mathbf{u}_E with $\mathbf{v}(\mathbf{k})$ to obtain the so-called momentum relaxation-time approximation (mRTA) for the scattering time:

$$\frac{1}{\tau_{\text{mRTA}}(\mathbf{k})} = \sum_{\mathbf{k}'} P_{\mathbf{k}\mathbf{k}'} \frac{1 - f^0(\mathbf{k}')}{1 - f^0(\mathbf{k})} \times \left\{ 1 - \frac{\mathbf{v}(\mathbf{k}') \cdot \mathbf{v}(\mathbf{k})}{\mathbf{v}(\mathbf{k})^2} \right\}, \quad (\text{A3})$$

which gives very similar results. If the second term in brackets on the right-hand side is neglected, we finally obtain the scattering time within the energy relaxation-time approximation (eRTA):

$$\frac{1}{\tau_{\text{eRTA}}(\mathbf{k})} = \sum_{\mathbf{k}'} P_{\mathbf{k}\mathbf{k}'} \frac{1 - f^0(\mathbf{k}')}{1 - f^0(\mathbf{k})} \quad (\text{A4})$$

II. ALTERNATIVE ALGEBRAIC SOLUTION TO THE BTE

We give here an other method to solve the BTE, relying on a direct algebraic solution of the system. Writing the BTE for the N_i irreducible states yields N_i equations and N_f unknown variables $\tau(\mathbf{k}')$. To solve the corresponding system, we first need to fold it back on the irreducible states, using the fact that $\tau(\mathbf{k}') \approx \tau(\tilde{\mathbf{k}}')$ where $\tilde{\mathbf{k}}' \in \mathcal{I}$ is the symmetry equivalent of $\mathbf{k}' \in \mathcal{F}$:

$$\begin{aligned} & (1 - f^0(\tilde{\mathbf{k}})) \mathbf{v}(\tilde{\mathbf{k}}) \cdot \mathbf{u}_E = \\ & \sum_{\mathbf{k}'} P_{\tilde{\mathbf{k}}\mathbf{k}'} (1 - f^0(\mathbf{k}')) \mathbf{v}(\tilde{\mathbf{k}}) \cdot \mathbf{u}_E \times \tau(\tilde{\mathbf{k}}) \\ & - \sum_{\tilde{\mathbf{k}}'} \left(\sum_{\mathbf{k}' \equiv \tilde{\mathbf{k}}'} P_{\tilde{\mathbf{k}}\mathbf{k}'} (1 - f^0(\mathbf{k}')) \times \mathbf{v}(\mathbf{k}') \cdot \mathbf{u}_E \right) \tau(\tilde{\mathbf{k}}'). \end{aligned} \quad (\text{A5})$$

From there we use the same techniques mentioned in the main text to have a well-behaved set of N_i equations with N_i unknowns. Written as a matrix-vector product, it reads:

$$\forall \tilde{\mathbf{k}} \in \mathcal{I}, F_{\tilde{\mathbf{k}}} = \sum_{\tilde{\mathbf{k}}'} \mathcal{S}_{\tilde{\mathbf{k}}, \tilde{\mathbf{k}}'} \tau_{\tilde{\mathbf{k}}'}, \quad (\text{A6})$$

where

$$F_{\tilde{\mathbf{k}}} = (1 - f^0(\tilde{\mathbf{k}})) \mathbf{v}(\tilde{\mathbf{k}}) \cdot \mathbf{u}_{\tilde{\mathbf{k}}} \quad (\text{A7})$$

$$\begin{aligned} \mathcal{S}_{\tilde{\mathbf{k}}, \tilde{\mathbf{k}}'} &= \left(\sum_{\mathbf{k}''} P_{\tilde{\mathbf{k}}\mathbf{k}''} (1 - f^0(\mathbf{k}'')) \mathbf{v}(\tilde{\mathbf{k}}) \cdot \mathbf{u}_{\tilde{\mathbf{k}}} \right) \delta_{\tilde{\mathbf{k}}, \tilde{\mathbf{k}}'} \\ &- \left(\sum_{\mathbf{k}' \equiv \tilde{\mathbf{k}}'} P_{\tilde{\mathbf{k}}\mathbf{k}'} (1 - f^0(\mathbf{k}')) \times \mathbf{v}(\mathbf{k}') \cdot \mathbf{u}_{\tilde{\mathbf{k}}} \right) \end{aligned} \quad (\text{A8})$$

Solving the BTE then boils down to a matrix inversion, and this gives us the values of τ on the \mathcal{I} grid. It is then rotated according to the symmetries of the band structure, and interpolated linearly on the fine grid of the pockets \mathcal{F} . In this approach, the δ functions in Eq. 4 are replaced by Gaussians, and a convergence test is performed on the associated broadening. This way, one associates a weight to each contribution from each \mathbf{k} point, and the contributions can then be organized as a matrix. In the triangles method, one does not associate a contribution to each \mathbf{k} point of the grid. For the integral to be computed, the integrand must be known a priori. This is not the case here since the integrals involve the scattering times at all \mathbf{k} . The approach discussed here and the one in the main text give the same results within a 5% error, provided the broadening parameter is chosen properly.

III. BANDS STRUCTURES AND PHONON DISPERSIONS

For the materials studied here, we report the band structures in Fig. A1, phonon dispersions in Fig. A2 and some interesting quantities related to the band structures in Table I.

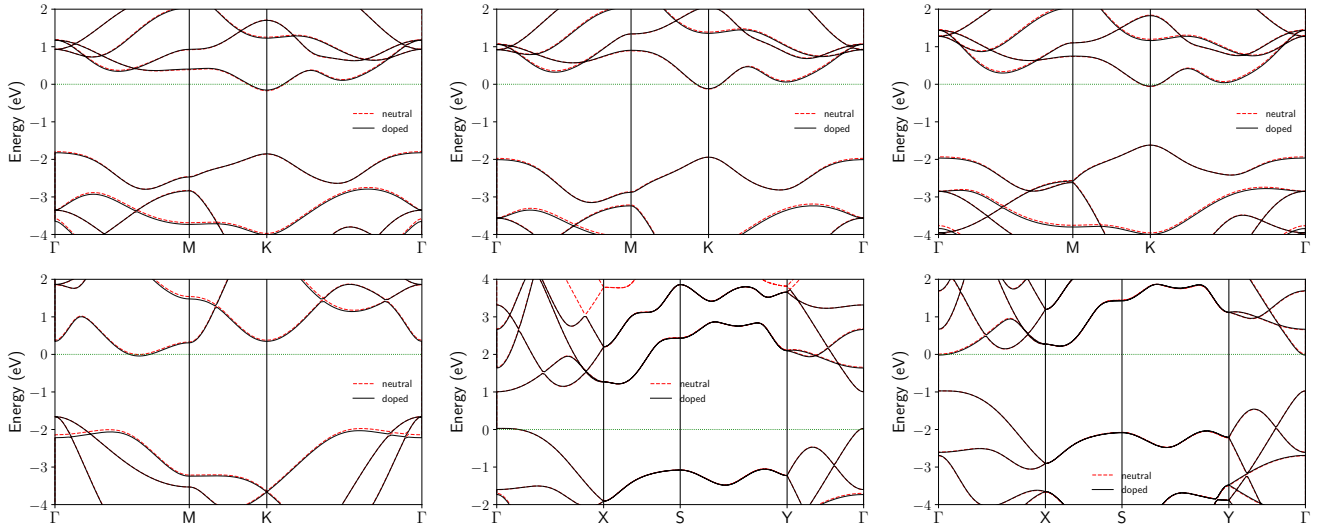


FIG. A1. From left to right, top to bottom: band structure along high symmetry path for electron-doped MoS₂, WS₂, and WSe₂, As, P₄, and hole-doped P₄ (black solid lines) compared with the undoped case (red dashed lines). In each case the band structures are aligned with respect to the top of the valence band. The zero is at the Fermi level of the doped case.

TABLE I. Extracted quantitative characteristics of the band structures. The first column shows effective masses at the band edges relevant for transport, obtained from finite-differences differentiation. If the effective mass is anisotropic the lighter effective mass is indicated as transport effective mass (T) while the mass in the perpendicular direction is referred to as longitudinal mass (L). The second column shows the absolute energy difference between the bottom of the conduction band (top of the valence band) and the Fermi level. The third column shows the absolute energy difference between the bottom of the K valley and the bottom of the Q valley in TMDs.

Material (e or h doped)	Effective masses (m_0)	$\Delta(E_{Fermi} - E_{max,min})(meV)$	$\Delta(E_K - E_Q)(meV)$
MoS2(e)	$m_K^* = 0.417$	153.3	257.4
WS2(e)	$m_K^* = 0.314$	118.1	178.0
WSe2(e)	$m_K^* = 0.330$	50.2	92.0
As(e)	$m_Q^*(T) = 0.145, m_Q^*(L) = 0.517$	42.8	-
P (h)	$m_\Gamma^*(T) = 0.172, m_\Gamma^*(L) = 8.872$	28.9	-
P (e)	$m_\Gamma^*(T) = 0.139, m_\Gamma^*(L) = 1.237$	18.9	-

IV. ADDITIONAL EPC PLOTS:

Here we show additional plots for the EPC matrix elements of MoS₂, WS₂, WSe₂ and phosphorene.

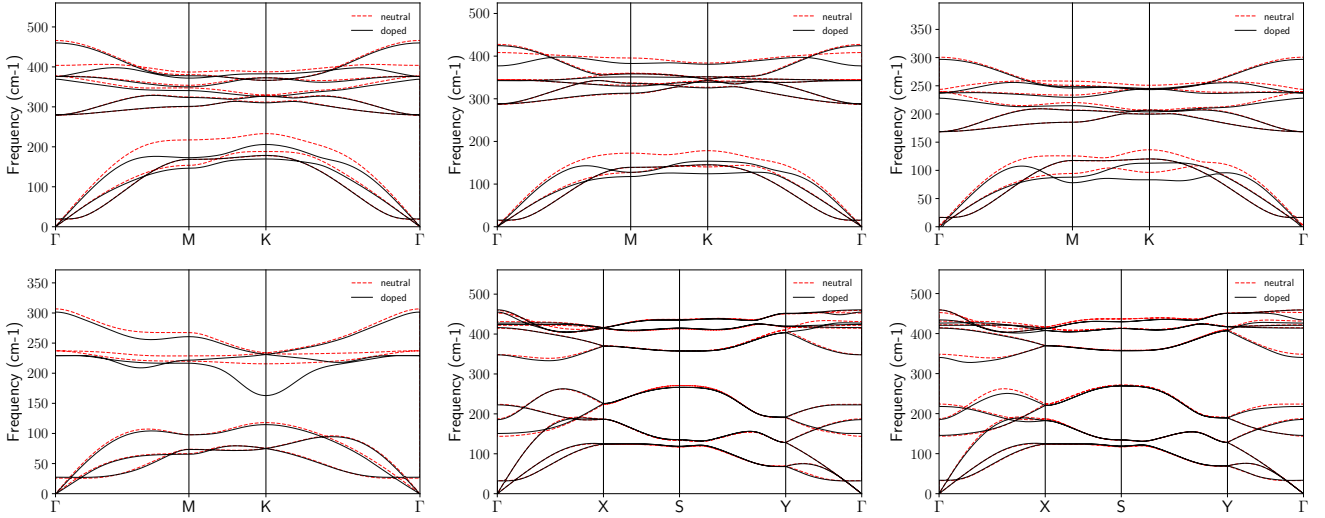


FIG. A2. From left to right, top to bottom: phonon dispersion along high symmetry path for electron-doped MoS₂, WS₂, and WSe₂, As, P₄, and hole-doped P₄ (black solid lines) compared with the undoped case (red dashed lines). Phonon softenings can be observed for phonons corresponding to possible electronic transitions with strong electron-phonon coupling. For example, in arsenene, the softening at K corresponds to the strong intervalley coupling ($g \approx 140$ meV) with mode number 4 observed in Fig. 4.

- ¹ D. K. Efetov and P. Kim, *Controlling Electron-Phonon Interactions in Graphene at Ultrahigh Carrier Densities*, Physical Review Letters **105**, 256805 (2010).
- ² B. Radisavljevic, A. Radenovic, J. Brivio, V. Giacometti, and A. Kis, *Single-layer MoS₂ transistors*, Nature Nanotechnology **6**, 147 (2011).
- ³ S. Lebègue, T. Björkman, M. Klintonberg, R. M. Nieminen, and O. Eriksson, *Two-Dimensional Materials from Data Filtering and Ab Initio Calculations*, Phys. Rev. X **3**, 031002 (2013).
- ⁴ D. Hanlon, C. Backes, E. Doherty, C. S. Cucinotta, N. C. Berner, C. Boland, K. Lee, A. Harvey, P. Lynch, Z. Gholamvand, S. Zhang, K. Wang, G. Moynihan, A. Pokle, Q. M. Ramasse, N. McEvoy, W. J. Blau, J. Wang, G. Abellan, F. Hauke, A. Hirsch, S. Sanvito, D. D. O'Regan, G. S. Duesberg, V. Nicolosi, and J. N. Coleman, *Liquid exfoliation of solvent-stabilized few-layer black phosphorus for applications beyond electronics*, Nature Communications **6**, 8563 (2015).
- ⁵ P. Yasaei, B. Kumar, T. Foroozan, C. Wang, M. Asadi, D. Tuschel, J. E. Indacochea, R. F. Klie, and A. Salehi-Khojin, *High-Quality Black Phosphorus Atomic Layers by Liquid-Phase Exfoliation*, Advanced Materials **27**, 1887 (2015).
- ⁶ C. Gibaja, D. Rodriguez-San-Miguel, P. Ares, J. Gómez-Herrero, M. Varela, R. Gillen, J. Maultzsch, F. Hauke, A. Hirsch, G. Abellán, and F. Zamora, *Few-Layer Antimonene by Liquid-Phase Exfoliation*, Angewandte Chemie International Edition **55**, 14345 (2016).
- ⁷ P. Ares, F. Aguilar-Galindo, D. Rodríguez-San-Miguel, D. A. Aldave, S. Díaz-Tendero, M. Alcamí, F. Martín, J. Gómez-Herrero, and F. Zamora, *Mechanical Isolation of Highly Stable Antimonene under Ambient Conditions*, Advanced Materials **28**, 6332 (2016).
- ⁸ D. A. Bandurin, A. V. Tyurnina, G. L. Yu, A. Mishchenko, V. Zólyomi, S. V. Morozov, R. K. Kumar, R. V. Gorbachev, Z. R. Kudrynskiy, S. Pezzini, Z. D. Kovalyuk, U. Zeitler, K. S. Novoselov, A. Patané, L. Eaves, I. V. Grigorieva, V. I. Fal'ko, A. K. Geim, and Y. Cao, *High electron mobility, quantum Hall effect and anomalous optical response in atomically thin InSe*, Nature Nanotechnology **12**, 223 EP (2016).
- ⁹ M. Ashton, J. Paul, S. B. Sinnott, and R. G. Hennig, *Topology-Scaling Identification of Layered Solids and Stable Exfoliated 2D Materials*, Phys. Rev. Lett. **118**, 106101 (2017).
- ¹⁰ G. Cheon, K.-A. N. Duerloo, A. D. Sendek, C. Porter, Y. Chen, and E. J. Reed, *Data Mining for New Two- and One-Dimensional Weakly Bonded Solids and Lattice-Commensurate Heterostructures*, Nano Letters **17**, 1915 (2017).
- ¹¹ N. Mounet, M. Gibertini, P. Schwaller, D. Campi, A. Merkys, A. Marrazzo, Thib, I. E. Castelli, A. Cepellotti, G. Pizzi, and N. Marzari, *Two-dimensional materials from high-throughput computational exfoliation of experimentally known compounds*, Nature Nanotechnology **13**, 246 (2018).
- ¹² Q. H. Wang, K. Kalantar-Zadeh, A. Kis, J. N. Coleman, and M. S. Strano, *Electronics and optoelectronics of two-dimensional transition metal dichalcogenides*, Nat. Nanotech. **7**, 699 (2012).

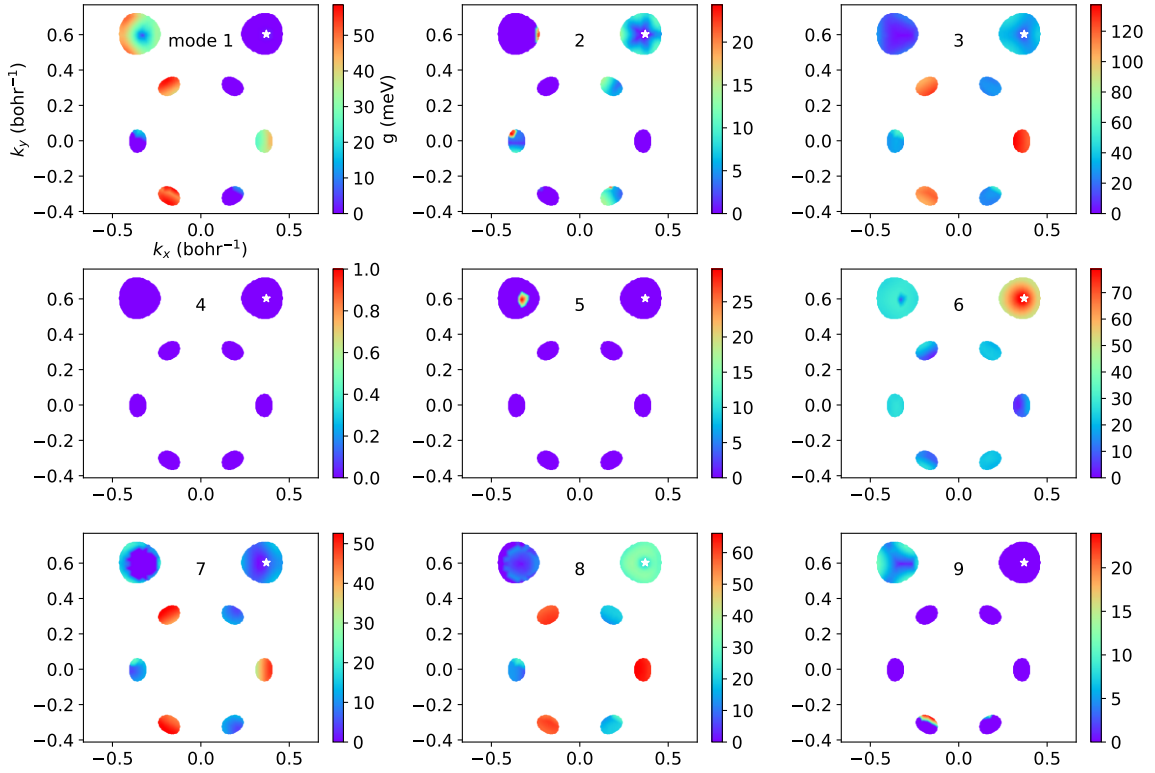


FIG. A3. Interpolated $g_{\mathbf{k}\mathbf{k}'}$ for electron-doped MoS₂. The initial state considered is indicated by a white star. The rest of the points are the possible final states in the finely sampled pockets and the color of the point indicates the strength of the electron-phonon coupling matrix element. The index of the phonon mode indicated at the top of each subplot refers to a purely energetic ordering of the phonon modes associated with each transition.

- ¹³ M. Chhowalla, D. Jena, and H. Zhang, *Two-dimensional semiconductors for transistors*, Nature Reviews Materials **1**, 16052 (2016).
- ¹⁴ J. M. Ziman, *Electrons and phonons: the theory of transport phenomena in solids* (Clarendon, Oxford, 1960).
- ¹⁵ P. B. Allen, *New Method for Solving Boltzmann's equation for electrons in metals*, Physical Review B **17**, 3725 (1978).
- ¹⁶ G. Grimvall, *The electron-phonon interaction in metals* (North-Holland, Amsterdam, 1981).
- ¹⁷ F. Giustino, *Electron-phonon interactions from first principles*, Reviews of Modern Physics **89**, 015003 (2017).
- ¹⁸ S. Y. Savrasov, D. Y. Savrasov, and O. K. Andersen, *Linear-response calculations of electron-phonon interactions*, Phys. Rev. Lett. **72**, 372 (1994).
- ¹⁹ A. Y. Liu and A. A. Quong, *Linear-response calculation of electron-phonon coupling parameters*, Phys. Rev. B **53**, R7575 (1996).
- ²⁰ F. Mauri, O. Zakharov, S. de Gironcoli, S. G. Louie, and M. L. Cohen, *Phonon Softening and Superconductivity in Tellurium under Pressure*, Phys. Rev. Lett. **77**, 1151 (1996).
- ²¹ R. Bauer, A. Schmid, P. Pavone, and D. Strauch, *Electron-phonon coupling in the metallic elements Al, Au, Na, and Nb: A first-principles study*, Phys. Rev. B **57**, 11276 (1998).
- ²² S. Baroni, S. de Gironcoli, A. Dal Corso, and P. Giannozzi, *Phonons and related crystal properties from density-functional perturbation theory*, Rev. Mod. Phys. **73**, 515 (2001).
- ²³ M. M. Dacorogna, M. L. Cohen, and P. K. Lam, *Self-Consistent Calculation of the q Dependence of the Electron-Phonon Coupling in Aluminum*, Phys. Rev. Lett. **55**, 837 (1985).
- ²⁴ T. Gunst, T. Markussen, K. Stokbro, and M. Brandbyge, *First-principles method for electron-phonon coupling and electron mobility: Applications to two-dimensional materials*, Physical Review B **93**, 035414 (2016).
- ²⁵ T. Sohler, M. Calandra, and F. Mauri, *Two-dimensional Fröhlich interaction in transition-metal dichalcogenide monolayers: Theoretical modeling and first-principles calculations*, Physical Review B **94**, 085415 (2016).
- ²⁶ B. Kozinsky and N. Marzari, *Static Dielectric Properties of Carbon Nanotubes from First Principles*, Physical Review Letters **96**, 166801 (2006).
- ²⁷ T. Sohler, M. Calandra, and F. Mauri, *Density-functional calculation of static screening in two-dimensional materials: The long-wavelength dielectric function of graphene*, Phys. Rev. B **91**, 165428 (2015).
- ²⁸ T. Sohler, M. Gibertini, M. Calandra, F. Mauri, and N. Marzari, *Breakdown of Optical Phonons' Splitting in Two-Dimensional Materials*, Nano Letters **17**, 3758 (2017).
- ²⁹ T. Sohler, M. Calandra, and F. Mauri, *Density functional perturbation theory for gated two-dimensional heterostructures: Theoretical developments and application to flexural phonons in graphene*, Physical Review B **96**, 075448 (2017).

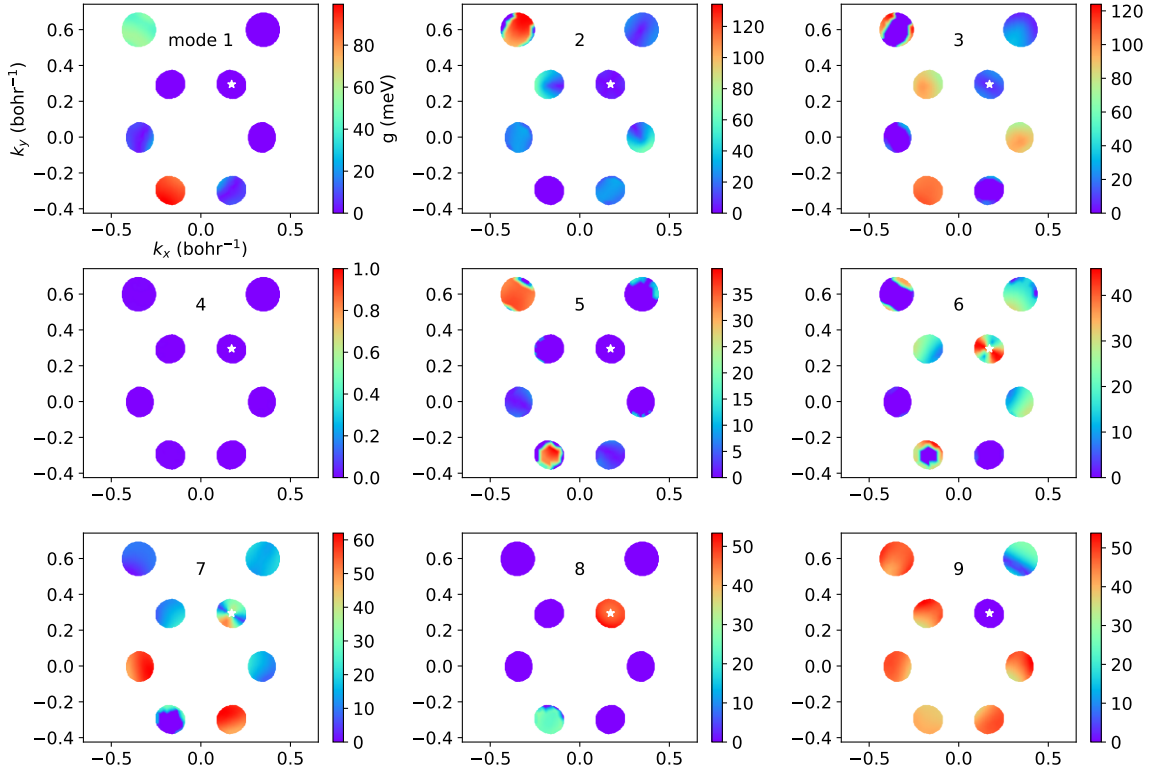


FIG. A4. Interpolated $g_{\mathbf{k}\mathbf{k}'}$ for electron-doped WS_2 , with the initial state at the bottom of the Q valley.

- ³⁰ Y. S. Lee, M. Buongiorno Nardelli, and N. Marzari, *Band structure and quantum conductance of nanostructures from maximally localized Wannier functions: The case of functionalized carbon nanotubes*, Physical Review Letters **95**, 076804 (2005).
- ³¹ J. R. Yates, X. Wang, D. Vanderbilt, and I. Souza, *Spectral and Fermi surface properties from Wannier interpolation*, Physical Review B **75**, 195121 (2007).
- ³² F. Giustino, M. L. Cohen, and S. G. Louie, *Electron-phonon interaction using Wannier functions*, Phys. Rev. B **76**, 165108 (2007).
- ³³ M. Calandra, G. Profeta, and F. Mauri, *Adiabatic and nonadiabatic phonon dispersion in a Wannier function approach*, Phys. Rev. B **82**, 165111 (2010).
- ³⁴ N. Marzari, A. A. Mostofi, J. R. Yates, I. Souza, and D. Vanderbilt, *Maximally localized Wannier functions: Theory and applications*, Rev. Mod. Phys. **84**, 1419 (2012).
- ³⁵ S. Ponc e, E. Margine, C. Verdi, and F. Giustino, *EPW: Electron-phonon coupling, transport and superconducting properties using maximally localized Wannier functions*, Computer Physics Communications **209**, 116 (2016).
- ³⁶ J. Sjakste, N. Vast, M. Calandra, and F. Mauri, *Wannier interpolation of the electron-phonon matrix elements in polar semiconductors: Polar-optical coupling in GaAs*, Phys. Rev. B **92**, 054307 (2015).
- ³⁷ C. Verdi and F. Giustino, *Fr ohlich Electron-Phonon Vertex from First Principles*, Phys. Rev. Lett. **115**, 176401 (2015).
- ³⁸ S. Y. Savrasov and D. Y. Savrasov, *Electron-phonon interactions and related physical properties of metals from linear-response theory*, Phys. Rev. B **54**, 16487 (1996).
- ³⁹ O. D. Restrepo, K. Varga, and S. T. Pantelides, *First-principles calculations of electron mobilities in silicon: Phonon and Coulomb scattering*, Applied Physics Letters **94**, 212103 (2009).
- ⁴⁰ R. S. Shishir and D. K. Ferry, *Intrinsic mobility in graphene.*, Journal of physics. Condensed matter : An Institute of Physics journal **21**, 232204 (2009).
- ⁴¹ K. M. Borysenko, J. T. Mullen, E. A. Barry, S. Paul, Y. G. Semenov, J. M. Zavada, M. Buongiorno Nardelli, and K. W. Kim, *First-principles analysis of electron-phonon interactions in graphene*, Physical Review B **81**, 121412 (2010).
- ⁴² Z. Jin, X. Li, J. T. Mullen, and K. W. Kim, *Intrinsic transport properties of electrons and holes in monolayer transition-metal dichalcogenides*, Physical Review B **90**, 045422 (2014).
- ⁴³ O. D. Restrepo, K. E. Krymowski, J. Goldberger, and W. Windl, *A first principles method to simulate electron mobilities in 2D materials*, New Journal of Physics **16** (2014).
- ⁴⁴ C.-H. Park, N. Bonini, T. Sohier, G. Samsonidze, B. Kozinsky, M. Calandra, F. Mauri, and N. Marzari, *Electron-Phonon Interactions and the Intrinsic Electrical Resistivity of Graphene.*, Nano letters **14**, 1113 (2014).
- ⁴⁵ Z. Jin, J. T. Mullen, and K. W. Kim, *Highly anisotropic electronic transport properties of monolayer and bilayer phosphorene from first principles*, Applied Physics Letters **109**, 053108 (2016).
- ⁴⁶ A. N. Rudenko, S. Brener, and M. I. Katsnelson, *Intrinsic Charge Carrier Mobility in Single-Layer Black Phosphorus*, Physical Review Letters **116**, 246401 (2016).

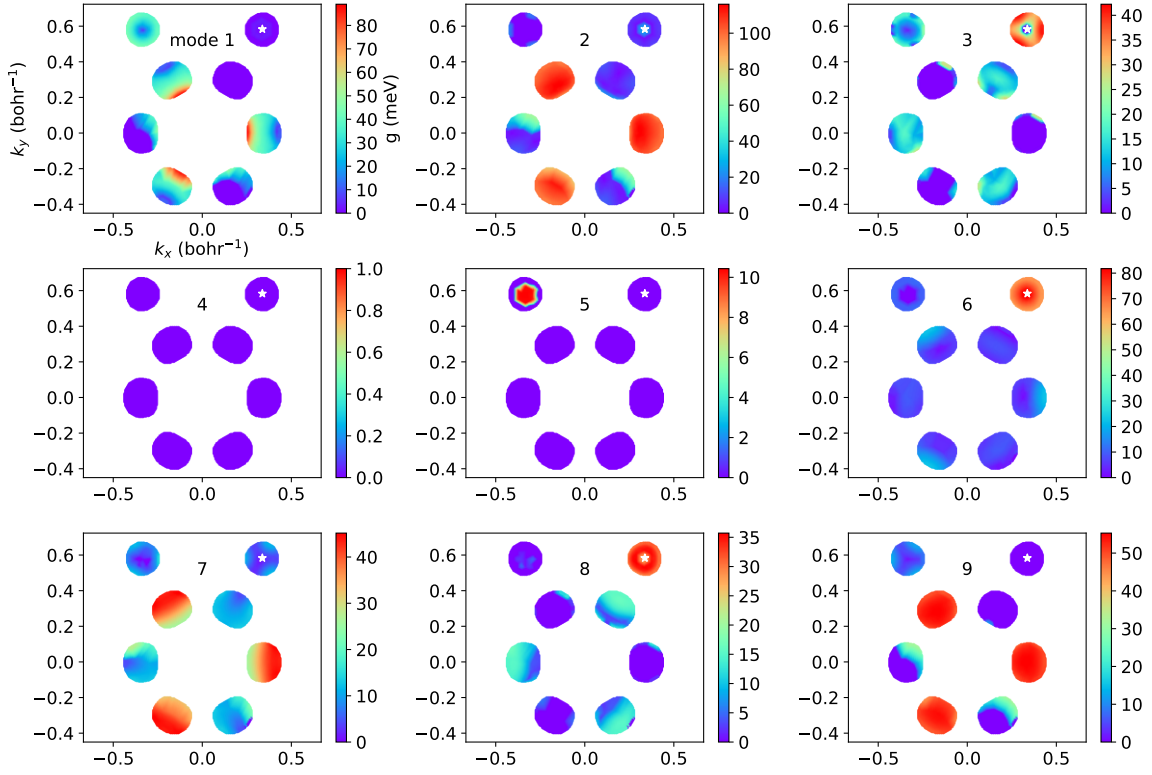


FIG. A5. Interpolated $g_{\mathbf{k}\mathbf{k}'}$ for electron-doped WSe₂, with the initial state at the bottom of the K valley.

- ⁴⁷ Y. Trushkov and V. Perebeinos, *Phonon-limited carrier mobility in monolayer black phosphorus*, Physical Review B **95**, 075436 (2017).
- ⁴⁸ G. Gaddemane, W. G. Vandenberghe, M. L. Van de Put, S. Chen, S. Tiwari, E. Chen, and M. V. Fischetti, *Theoretical studies of electronic transport in monolayer and bilayer phosphorene: A critical overview*, Phys. Rev. B **98**, 115416 (2018).
- ⁴⁹ S. Ponc e, E. R. Margine, and F. Giustino, *Towards predictive many-body calculations of phonon-limited carrier mobilities in semiconductors*, Physical Review B **97** (2018).
- ⁵⁰ D. L. Rode, *Electron Mobility in Direct-Gap Polar Semiconductors*, Phys. Rev. B **2**, 1012 (1970).
- ⁵¹ D. L. Rode, *Electron Mobility in II-VI Semiconductors*, Phys. Rev. B **2**, 4036 (1970).
- ⁵² K. Kaasbjerg, K. S. Thygesen, and K. W. Jacobsen, *Phonon-limited mobility in n-type single-layer MoS₂ from first principles*, Physical Review B **85**, 115317 (2012).
- ⁵³ K. Kaasbjerg, K. S. Thygesen, and A.-P. P. Jauho, *Acoustic phonon limited mobility in two-dimensional semiconductors: Deformation potential and piezoelectric scattering in monolayer MoS₂ from first principles*, Physical Review B **87**, 235312 (2013).
- ⁵⁴ W. Li, *Electrical transport limited by electron-phonon coupling from Boltzmann transport equation: An ab initio study of Si, Al, and MoS₂*, Physical Review B **92**, 075405 (2015).
- ⁵⁵ J. Ma, A. S. Nissimagoudar, and W. Li, *First-principles study of electron and hole mobilities of Si and GaAs*, Phys. Rev. B **97**, 045201 (2018).
- ⁵⁶ M. Fiorentini and N. Bonini, *Thermoelectric coefficients of n-doped silicon from first principles via the solution of the Boltzmann transport equation*, Phys. Rev. B **94**, 085204 (2016).
- ⁵⁷ G. Fugallo, M. Lazzeri, L. Paulatto, and F. Mauri, *Ab initio variational approach for evaluating lattice thermal conductivity*, Phys. Rev. B **88**, 045430 (2013).
- ⁵⁸ G. Fugallo, A. Cepellotti, L. Paulatto, M. Lazzeri, N. Marzari, and F. Mauri, *Thermal Conductivity of Graphene and Graphite: Collective Excitations and Mean Free Paths*, Nano Letters **14**, 6109 (2014).
- ⁵⁹ A. Cepellotti, G. Fugallo, L. Paulatto, M. Lazzeri, F. Mauri, and N. Marzari, *Phonon hydrodynamics in two-dimensional materials*, Nature Communications **6**, 6400 (2015).
- ⁶⁰ T. Sohler, M. Calandra, C.-H. Park, N. Bonini, N. Marzari, and F. Mauri, *Phonon-limited resistivity of graphene by first-principles calculations: Electron-phonon interactions, strain-induced gauge field, and Boltzmann equation*, Physical Review B **90**, 125414 (2014).
- ⁶¹ J. A. Ashraff and P. D. Loly, *The triangular linear analytic method for two-dimensional spectral functions*, Journal of Physics C: Solid State Physics **20**, 4823 (1987).
- ⁶² T. G. Pedersen, C. Flindt, J. Pedersen, A.-P. Jauho, N. A. Mortensen, and K. Pedersen, *Optical properties of graphene antidot lattices*, Phys. Rev. B **77**, 245431 (2008).
- ⁶³ T. Ando, *Screening Effect and Impurity Scattering in Monolayer Graphene*, Journal of the Physics Society of Japan **75**, 074716 (2006).
- ⁶⁴ E. H. Hwang, S. Adam, and S. Das Sarma, *Carrier Transport in Two-Dimensional Graphene Layers*, Physical Review Letters **98**, 186806 (2007).
- ⁶⁵ J. L. Manes, *Symmetry-based approach to electron-phonon interactions in graphene*, Physical Review B **76**, 045430 (2007).

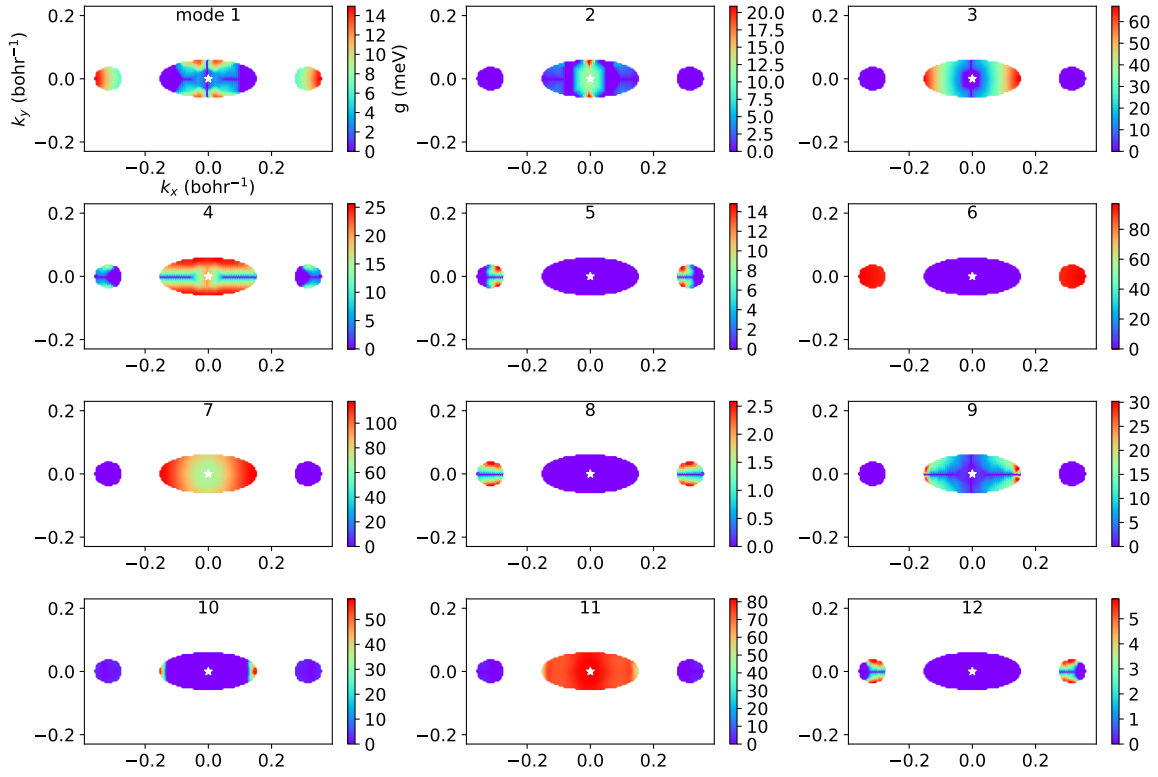


FIG. A6. Interpolated $g_{\mathbf{k}\mathbf{k}'}$ for electron-doped phosphorene, with the initial state at the bottom of the Γ valley.

- (2007).
- ⁶⁶ G. G. Samsonidze, E. B. Barros, R. Saito, J. Jiang, G. Dresselhaus, and M. S. Dresselhaus, *Electron-phonon coupling mechanism in two-dimensional graphite and single-wall carbon nanotubes*, Physical Review B **75**, 155420 (2007).
- ⁶⁷ T. Stauber, N. Peres, and F. Guinea, *Electronic transport in graphene: A semiclassical approach including midgap states*, Physical Review B **76**, 205423 (2007).
- ⁶⁸ S. Fratini and F. Guinea, *Substrate-limited electron dynamics in graphene*, Physical Review B **77**, 195415 (2008).
- ⁶⁹ E. H. Hwang and S. Das Sarma, *Acoustic phonon scattering limited carrier mobility in two-dimensional extrinsic graphene*, Physical Review B **77**, 115449 (2008).
- ⁷⁰ E. H. Hwang, S. D. Sarma, and S. Das Sarma, *Screening-induced temperature-dependent transport in two-dimensional graphene*, Physical Review B **79**, 165404 (2009).
- ⁷¹ E. Mariani and F. von Oppen, *Temperature-dependent resistivity of suspended graphene*, Physical Review B **82**, 195403 (2010).
- ⁷² S. Das Sarma, S. Adam, E. H. Hwang, and E. Rossi, *Electronic transport in two-dimensional graphene*, Reviews of Modern Physics **83**, 407 (2011).
- ⁷³ K. Kaasbjerg, K. K. Thygesen, and K. K. Jacobsen, *Unraveling the acoustic electron-phonon interaction in graphene*, Physical Review B **85**, 165440 (2012).
- ⁷⁴ S. Das Sarma and E. H. Hwang, *Density-dependent electrical conductivity in suspended graphene: Approaching the Dirac point in transport*, Physical Review B **87**, 035415 (2013).
- ⁷⁵ T. Gunst, K. Kaasbjerg, and M. Brandbyge, *Flexural-Phonon Scattering Induced by Electrostatic Gating in Graphene*, Physical Review Letters **118**, 046601 (2017).
- ⁷⁶ J. Qiao, X. Kong, Z.-X. Hu, F. Yang, and W. Ji, *High-mobility transport anisotropy and linear dichroism in few-layer black phosphorus*, Nature Communications **5**, 4475 (2014).
- ⁷⁷ B. Liao, J. Zhou, B. Qiu, M. S. Dresselhaus, and G. Chen, *Ab initio study of electron-phonon interaction in phosphorene*, Physical Review B **91**, 235419 (2015).
- ⁷⁸ Y. Wang and Y. Ding, *Electronic Structure and Carrier Mobilities of Arsenene and Antimonene Nanoribbons: A First-Principle Study*, Nanoscale Research Letters **10**, 254 (2015).
- ⁷⁹ G. Pizzi, M. Gibertini, E. Dib, N. Marzari, G. Iannaccone, and G. Fiori, *Performance of arsenene and antimonene double-gate MOSFETs from first principles*, Nature Communications **7**, 1258 (2016).
- ⁸⁰ Y. Wang, P. Huang, M. Ye, R. Quhe, Y. Pan, H. Zhang, H. Zhong, J. Shi, and J. Lu, *Many-body Effect, Carrier Mobility, and Device Performance of Hexagonal Arsenene and Antimonene*, Chemistry of Materials **29**, 2191 (2017).
- ⁸¹ N. W. Ashcroft and N. D. Mermin, *Solid State Physics* (Brooks Cole, Belmont (USA), 1976) ISBN 0030839939.
- ⁸² B. Nag, *Electron Transport in Compound Semiconductors*, Springer Series in Solid-State Sciences, Springer Series in Solid-State Sciences **11** (1980).
- ⁸³ O. Gritsenko, R. van Leeuwen, E. van Lenthe, and E. Baerends, *Self-consistent approximation to the Kohn-Sham exchange potential*, Physical Review A **51**, 1944 (1995).

- ⁸⁴ M. Kuisma, J. Ojanen, J. Enkovaara, and T. Rantala, *Kohn-Sham potential with discontinuity for band gap materials*, Physical Review B **82**, 115106 (2010).
- ⁸⁵ M. L. Cohen and T. K. Bergstresser, *Band Structures and Pseudopotential Form Factors for Fourteen Semiconductors of the Diamond and Zinc-blende Structures*, Physical Review **141**, 789 (1966).
- ⁸⁶ L.-W. Wang and A. Zunger, *Local-density-derived semiempirical pseudopotentials*, Physical Review B **51**, 17398 (1995).
- ⁸⁷ P. Giannozzi, O. Andreussi, T. Brumme, O. Bunau, M. Buongiorno Nardelli, M. Calandra, R. Car, C. Cavazzoni, D. Ceresoli, M. Cococcioni, N. Colonna, I. Carnimeo, A. Dal Corso, S. de Gironcoli, P. Delugas, R. A. DiStasio, A. Ferretti, A. Floris, G. Fratesi, G. Fugallo, R. Gebauer, U. Gerstmann, F. Giustino, T. Gorni, J. Jia, M. Kawamura, H.-Y. Ko, A. Kokalj, E. Küçükbenli, M. Lazzeri, M. Marsili, N. Marzari, F. Mauri, N. L. Nguyen, H.-V. Nguyen, A. Otero-de-la Roza, L. Paulatto, S. Poncé, D. Rocca, R. Sabatini, B. Santra, M. Schlipf, A. P. Seitsonen, A. Smogunov, I. Timrov, T. Thonhauser, P. Umari, N. Vast, X. Wu, and S. Baroni, *Advanced capabilities for materials modelling with Quantum ESPRESSO*, Journal of Physics: Condensed Matter **29**, 465901 (2017).
- ⁸⁸ P. Giannozzi, S. Baroni, N. Bonini, M. Calandra, R. Car, C. Cavazzoni, D. Ceresoli, G. L. Chiarotti, M. Cococcioni, I. Dabo, A. Dal Corso, S. de Gironcoli, S. Fabris, G. Fratesi, R. Gebauer, U. Gerstmann, C. Gougousis, A. Kokalj, M. Lazzeri, L. Martin-Samos, N. Marzari, F. Mauri, R. Mazzarello, S. Paolini, A. Pasquarello, L. Paulatto, C. Sbraccia, S. Scandolo, G. Sclauzero, A. P. Seitsonen, A. Smogunov, P. Umari, and R. M. Wentzcovitch, *QUANTUM ESPRESSO: a modular and open-source software project for quantum simulations of materials.*, Journal of Physics: Condensed Matter **21**, 395502 (2009).
- ⁸⁹ C. A. Rozzi, D. Varsano, A. Marini, E. K. U. Gross, and A. Rubio, *Exact Coulomb cutoff technique for supercell calculations*, Phys. Rev. B **73**, 205119 (2006).
- ⁹⁰ S. Ismail-Beigi, *Truncation of periodic image interactions for confined systems*, Phys. Rev. B **73**, 233103 (2006).
- ⁹¹ G. Pizzi, A. Cepellotti, R. Sabatini, N. Marzari, and B. Kozinsky, *AiiDA: automated interactive infrastructure and database for computational science*, Computational Materials Science **111**, 218 (2016).
- ⁹² P. E. Blöchl, O. Jepsen, and O. K. Andersen, *Improved tetrahedron method for Brillouin-zone integrations*, Phys. Rev. B **49**, 16223 (1994).
- ⁹³ T. Brumme, M. Calandra, and F. Mauri, *First-principles theory of field-effect doping in transition-metal dichalcogenides: Structural properties, electronic structure, Hall coefficient, and electrical conductivity*, Physical Review B **91**, 155436 (2015).
- ⁹⁴ H. Shi, H. Pan, Y.-W. Zhang, and B. I. Yakobson, *Quasiparticle band structures and optical properties of strained monolayer MoS₂ and WS₂*, Physical Review B **87**, 155304 (2013).
- ⁹⁵ E. Maksimov and S. Shulga, *Nonadiabatic effects in optical phonon self-energy*, Solid State Communications **97**, 553 (1996).
- ⁹⁶ A. M. Saitta, M. Lazzeri, M. Calandra, and F. Mauri, *Giant Nonadiabatic Effects in Layer Metals: Raman Spectra of Intercalated Graphite Explained*, Phys. Rev. Lett. **100**, 226401 (2008).
- ⁹⁷ G. D. Mahan, *Electrons and phonons: the theory of transport phenomena in solids*, 3rd ed. (Plenum, New York, 2000).
- ⁹⁸ M. Lazzeri and F. Mauri, *Nonadiabatic Kohn Anomaly in a Doped Graphene Monolayer*, Phys. Rev. Lett. **97**, 266407 (2006).
- ⁹⁹ S. Pisana, M. Lazzeri, C. Casiraghi, K. S. Novoselov, A. K. Geim, A. C. Ferrari, and F. Mauri, *Breakdown of the adiabatic Born–Oppenheimer approximation in graphene*, Nature Materials **6**, 198 (2007).
- ¹⁰⁰ M. Lazzeri, C. Attaccalite, L. Wirtz, and F. Mauri, *Impact of the electron-electron correlation on phonon dispersion: Failure of LDA and GGA DFT functionals in graphene and graphite*, Phys. Rev. B **78**, 081406 (2008).
- ¹⁰¹ C. Verdi, F. Caruso, and F. Giustino, *Origin of the crossover from polarons to Fermi liquids in transition metal oxides*, Nature Communications **8**, 15769 (2017).
- ¹⁰² S. Z. Bisri, S. Shimizu, M. Nakano, and Y. Iwasa, *Endeavor of Iontronics: From Fundamentals to Applications of Ion-Controlled Electronics*, Advanced Materials **29**, 1607054 (2017).
- ¹⁰³ B. Y.-K. Hu and K. Flensberg, *Electron-electron scattering in linear transport in two-dimensional systems*, Phys. Rev. B **53**, 10072 (1996).
- ¹⁰⁴ F. Caruso and F. Giustino, *Theory of electron-plasmon coupling in semiconductors*, Phys. Rev. B **94**, 115208 (2016).
- ¹⁰⁵ G. Prandini, A. Marrazzo, I. E. Castelli, N. Mounet, and N. Marzari, *Precision and efficiency in solid-state pseudopotential calculations*, <http://www.materialscloud.org/sssp/>(2018).
- ¹⁰⁶ D. R. Hamann, *Optimized norm-conserving Vanderbilt pseudopotentials*, Physical Review B **88**, 085117 (2013).
- ¹⁰⁷ D. Vanderbilt, *Soft self-consistent pseudopotentials in a generalized eigenvalue formalism*, Physical Review B **41**, 7892 (1990).
- ¹⁰⁸ A. Dal Corso, *Pseudopotentials periodic table: From H to Pu*, Computational Materials Science **95**, 337 (2014).
- ¹⁰⁹ X. Li, J. T. Mullen, Z. Jin, K. M. Borysenko, M. Buongiorno Nardelli, and K. W. Kim, *Intrinsic electrical transport properties of monolayer silicene and MoS₂ from first principles*, Physical Review B **87**, 115418 (2013).
- ¹¹⁰ W. Zhang, Z. Huang, W. Zhang, and Y. Li, *Two-dimensional semiconductors with possible high room temperature mobility*, Nano research **7**, 1731 (2014).
- ¹¹¹ Z. Yu, Z. Y. Ong, Y. Pan, Y. Cui, R. Xin, Y. Shi, B. Wang, Y. Wu, T. Chen, Y. W. Zhang, G. Zhang, and X. Wang, *Realization of Room-Temperature Phonon-Limited Carrier Transport in Monolayer MoS₂ by Dielectric and Carrier Screening*, Advanced Materials **28**, 547 (2016).
- ¹¹² Z. Yu, Y. Pan, Y. Shen, Z. Wang, Z.-Y. Ong, T. Xu, R. Xin, L. Pan, B. Wang, L. Sun, J. Wang, G. Zhang, W. Y. Zhang, Y. Shi, and X. Wang, *Towards intrinsic charge transport in monolayer molybdenum disulfide by defect and interface engineering*, Nature Communications **5**, 5290 (2014).
- ¹¹³ B. Radisavljevic and A. Kis, *Mobility engineering and a metal–insulator transition in monolayer MoS₂*, Nature Materials **12**, 815 (2013).
- ¹¹⁴ S. Jo, N. Ubrig, H. Berger, A. B. Kuzmenko, and A. F. Morpurgo, *Mono- and Bilayer WS₂ Light-Emitting Transistors*, Nano Letters **14**, 2019 (2014).

- ¹¹⁵ D. Ovchinnikov, A. Allain, Y.-S. Huang, D. Dumcenco, and A. Kis, *Electrical Transport Properties of Single-Layer WS₂*, ACS Nano **8**, 8174 (2014).
- ¹¹⁶ A. S. Aji, P. Solís-Fernández, H. G. Ji, K. Fukuda, and H. Ago, *High Mobility WS₂ Transistors Realized by Multilayer Graphene Electrodes and Application to High Responsivity Flexible Photodetectors*, Advanced Functional Materials **27**, 1703448 (2017).
- ¹¹⁷ Y. Cui, R. Xin, Z. Yu, Y. Pan, Z.-Y. Ong, X. Wei, J. Wang, H. Nan, Z. Ni, Y. Wu, T. Chen, Y. Shi, B. Wang, G. Zhang, Y.-W. Zhang, and X. Wang, *High-Performance Monolayer WS₂ Field-Effect Transistors on High-k Dielectrics*, Advanced Materials **27**, 5230 (2015).
- ¹¹⁸ M. Z. Iqbal, M. Waqas and Iqbal, M. F. Khan, M. A. Shehzad, Y. Seo, J. H. Park, C. Hwang, and J. Eom, *High-mobility and air-stable single-layer WS₂ field-effect transistors sandwiched between chemical vapor deposition-grown hexagonal BN films*, Scientific Reports **5**, 10699 (2015).
- ¹¹⁹ J.-K. Huang, J. Pu, C.-L. Hsu, M.-H. Chiu, J. Zhen-Yu, Y.-H. Chang, W.-H. Chang, Y. Iwasa, T. Takenobu, and L.-J. Li, *Large-Area Synthesis of Highly Crystalline WSe₂ Monolayers and Device Applications*, ACS Nano **8**, 923 (2014).
- ¹²⁰ A. Allain and A. Kis, *Electron and Hole Mobilities in Single-Layer WSe₂*, ACS Nano **8**, 7180 (2014).
- ¹²¹ This number is estimated by solving the BTE for each mode successively, setting the coupling to the other modes to zero. This is simply an educated estimation. Indeed, the process is not strictly valid quantitatively since the solution to the BTE including all phonon modes is not the sum of the contributions from each mode.
- ¹²² B. Chakraborty, A. Bera, D. V. S. Muthu, S. Bhowmick, U. V. Waghmare, and A. K. Sood, *Symmetry-dependent phonon renormalization in monolayer MoS₂ transistor*, Physical Review B **85**, 161403 (2012).
- ¹²³ S. Takagi, A. Toriumi, M. Iwase, and H. Tango, *On the universality of inversion layer mobility in Si MOSFET's: Part II-effects of surface orientation*, IEEE Transactions on Electron Devices **41**, 2363 (1994).
- ¹²⁴ D. L. Rode and S. Knight, *Electron Transport in GaAs*, Phys. Rev. B **3**, 2534 (1971).
- ¹²⁵ J.-J. Zhou and M. Bernardi, *Ab initio electron mobility and polar phonon scattering in GaAs*, Phys. Rev. B **94**, 201201 (2016).